Main Manuscript for

Hadean-aged felsic sediments recycled through the deep mantle by early plate tectonics

Bradley J. Peters[1,*], Marc C. Halfar[1], Courtney J. Rundhaug[1,2], Paterno Castillo[3], Maria Schönbächler[1]

[1]Institute of Geochemistry and Petrology, ETH Zürich, 8092 Zürich, Switzerland

[2]Centre for Star and Planet Formation, University of Copenhagen, 1350 Copenhagen, Denmark

[3]Scripps Institution of Oceanography, University of California San Diego, La Jolla, CA 92093-0244, United States

*Corresponding author: bradley.peters@eaps.ethz.ch

Article major classification: Physical Sciences

Article minor category: Earth, Atmospheric, and Planetary Sciences

Keywords: mantle geochemistry, early Earth processes, mantle plumes, plate tectonics

Abstract word count: 237

Main text word count: 3388

Figures: 4

Supplementary text, figures, and tables accompany this article.

This manuscript has been submitted for consideration by *Proceedings of the National Academy of Sciences* after having undergone peer review at another journal.

Significance statement: The Marquesas volcanic hotspot contains a four-billion-year-old geochemical record of deep subduction of felsic sedimentary materials, implying that Earth's pathway to habitability through plate tectonics began very early in its history.

Abstract

The question of when modern tectonic processes arose on Earth has restricted our understanding of how and how quickly Earth reached its present, habitable form. Plate tectonics, and in particular deep subduction, is central to many facets of habitability: it controls heat flow, biogeochemical cycling, and creates a variety of marine and terrestrial biomes necessary for biological evolution. Many petrological, geodynamical, and geochemical perspectives have offered circumstantial evidence for both an early onset of plate tectonics, in the first 10% of Earth's history, or a late onset after the great oxidation event (2.5 Ga ago). We present geochemical data from the products of early subduction, which have been recycled into the deep mantle, stored for more than four billion years, and then tapped by the modern Marquesas volcanic hotspot. The felsic composition of these subducted materials requires that both crustal melting and sedimentation processes were active in some form before subduction took place. The early development of a mature plate tectonic system on Earth implies that its pathway to complex life was protracted: the foundations for habitability potentially began billions of years before the emergence of life. Emerging planetary bodies may, therefore, need long-term sustained plate tectonic processes to become host to complex biological systems. Further, the preservation of evidence for foundational planetary events in geologically young rocks reveals that Earth's volcanic hotspots could provide a defining perspective on the early planetary-scale processes that build Earth-like planets.

Introduction

Although the earliest part of Earth's geological history established the conditions required for habitability, the geological record from this period has been almost entirely lost. One central question about the Earth's earliest history is when it became habitable, which is in turn related to the initiation of deep biogeochemical cycles and climate stability through plate tectonics [1]. Subduction is accepted as a key element of plate tectonics, since it requires that sections of the lithosphere experienced mechanical strengthening, forming 'plates' that can coherently sink (subduct) in the mantle. While deep subduction (continuing at least to the mantle transition zone, i.e. >400 km deep) is understood to be a mostly self-sustaining process due to the pulling mechanism of subduction, it remains unclear how and when deep subduction initiated on Earth [2] and whether Archean tectonic regimes were characterized by shallow, rather than deep subduction [3].

There is broad agreement that the generation of felsic rocks on the early Earth is evidence that pre-existing mafic rocks were re-melted after being transported to subcrustal depths, possibly, although not necessarily by subduction [4]. Circumstantial evidence for the existence of early felsic crust, derived from its remaining mineral components [5, 6] or the residual composition of the mantle left behind during crustal building [7, 8], implies that rigid blocks resembling felsic continental plates were already being built as far back as 4.4 Ga ago. However, although the production of ancient felsic crust requires that mafic crust is buried and heated, the most common type of Archean felsic rock does not unambiguously require deep subduction similar to plate boundary processes observed today [9, 10]. Instead, there remains debate over whether subduction is required to build felsic crust [3, 6, 9], or whether subduction tectonics would even initially work against the stability of mature felsic crust [11].

The scarcity of Archean-aged rock representatives for subduction, such as ophiolites or high-pressure metamorphic rocks [12, 13], precludes direct study of subduction initiation in the early rock record. The preservation of Archean-aged orogenic rock assemblages has been used to infer an early onset of subduction [14], but neither documents subduction itself nor permits a direct comparison of potential Archean subduction to modern plate tectonics. Some petrological and geodynamical models have favored an early start of tectonic subduction (e.g., [6, 15]), but without primary evidence from the products of this subduction. A complementary perspective to studies of Archean-aged rocks is provided by Earth's volcanic hotspots, some of which have a geochemical memory that spans more than 4.5 billion years [16-18], which is longer than the longest lifespan of rocks on Earth's surface [19]. Volcanic hotspots are known to tap subducted materials from the deep mantle [20], which may have been stored there for

long geological timescales (≥ 2.5 Ga) [21] and may therefore preserve information about early tectonic processes. We present geochemical evidence from the Marquesas volcanic hotspot (southern Pacific Ocean) that subduction like that observed in modern plate tectonics was already active by the end of the Hadean Eon (ca. 4 Ga ago) and that it involved felsic geological materials akin to modern continental crust. Therefore, deep geochemical cycles critical to life on the modern Earth may have been established very early in Earth's history.

Mantle plumes as conduits for ancient geochemical signals

Many volcanic hotspots, like the Marquesas archipelago, are underlain by plumes that extend into the deep mantle [22]. The bases of many mantle plumes are associated with seismically anomalous domains in the deep mantle known as large low shear-wave velocity provinces (LLSVP); for example, the Pacific LLSVP lies under the Marquesas Islands. These LLSVP are commonly thought to represent stable thermochemical piles that may originate as dense primitive or subducted materials that accumulated at the base of the mantle [23-25]. The spatial association of these components leads to the joint tapping of primitive and subducted materials by volcanic hotspots in a process known as tectonic recycling [24]. In many hotspot sources, the subducted material represents altered oceanic crust, oceanic mantle lithosphere, and/or the overlying sediments that are coupled with oceanic crust during subduction (e.g., [26]). In only a few locations, including the Marquesas, the erupted lavas represent at least three subducted and primitive components that were mixed with each other before or during mantle melting (**Figure 1**) [27]. The Marquesas archipelago thus represents an ideal opportunity to directly compare the history of multiple geochemical components in the mantle. The distribution of these components among hotspot volcanoes often has a clear geographical structure sometimes referred to as compositional "stripes" that divide the various hotspot lavas into groups with distinct origins in the deep mantle [27]. The geochemical compositions exhibited by the components found in the Marquesas are not present in upper mantle-derived rocks, and the lack of a geochemically depleted, upper mantle component in Marquesas hotspot lavas strongly implies that their parental magmas are instead dominated by recycled, deep mantle components [27, 28].

The Marquesas hotspot is geochemically unique among global hotspots in that it appears to represent at least two mixing trends that each involve primitive material and either recycled oceanic crust (termed 'high-μ' or HIMU for its relatively high time-integrated $^{238}U/^{204}Pb$ signature) or subducted sediment (termed 'enriched mantle' or EM). It is commonly argued that the diverse geochemical signatures of EM-type hotspots (e.g., Pitcairn, Hawai'i, Kerguelen,

Samoa) represent an array of sedimentary origins, each of which may have a distinct origin or history [29]. However, the Marquesas hotspot does not display the extreme isotopic signatures reflected by other volcanic hotspots with HIMU (e.g., Mangaia) or EM (e.g., Samoa) componentry (**Figure 1**). The relatively diluted representation of these geochemical components in Marquesas lavas exacerbates the challenge of tracing the provenance of each component using long-lived radiogenic isotope systems (e.g., ^{87}Rb-^{87}Sr, ^{147}Sm-^{144}Nd, or ^{238}U-^{204}Pb) because the unique isotopic signatures are dampened by this dilution. This affects not only the isotopic signatures directly, but also indirectly by altering the parent-daughter ratios of each component's source.

The use of short-lived radiogenic systems, for which radioactive decay is restricted to the Hadean Eon (≥4 Ga old, i.e. the first ca. 10% of Earth's history) and thus long before such dilution, may simplify this issue by offering a binary perspective on the components of the Marquesas mantle source: heterogeneous short-lived radiogenic isotope signatures require incorporation of components with diverse Hadean-aged provenance, while homogeneous signatures do not require distinct Hadean-aged sources. The presence of ancient recycled materials in the Marquesas mantle source may have precluded the detection of heterogeneity in the short-lived ^{182}Hf-^{182}W radiogenic system [30], which has both lithophile (i.e. silicate-loving) and siderophile (i.e. metal-loving) properties. However, the exclusively lithophile nature of both Sm and Nd renders the short-lived ^{146}Sm-^{142}Nd system ($t_{1/2}$ = 103 Ma, [31]) more suitable for detecting Hadean-aged geochemical signatures in the Marquesas hotspot, since both its recycled and primitive components were formed through differentiation of silicate materials. Thus, if any of the geochemical components of the Marquesas hotspot were originally formed in the Hadean Eon, they may display heterogeneous ^{142}Nd/^{144}Nd ratios that can be measured with high-precision analysis techniques.

Distinct Hadean heritages for the Marquesas compositional components

Like the long-lived radiogenic signatures of Marquesas basalts, their μ^{142}Nd (^{142}Nd/^{144}Nd ratio normalized to the terrestrial standard, JNdi-1 [32], in parts per million) compositions reflect a geochemically heterogeneous source (**Figure 2**). Their μ^{142}Nd signatures range from -2.3 to +2.6 and reflect statistically significant heterogeneity (Supplementary Information). However, if the samples are divided into groups representing their geochemical componentry (**Figure 1**; Supplementary Information), each group instead reflects statistically homogeneous μ^{142}Nd compositions (**Figure 2**). Samples with EM-type isotopic compositions (hereafter the "EM group"; see Supplementary Information for a discussion of grouping)

display $\mu^{142}Nd$ = +2.3 ±1.3 (reported uncertainties always represent 95% confidence intervals calculated using Isoplot [33]; MSWD: 0.1, probability of fit: 0.87, *n* = 3), and those in the 'focal zone' (FOZO) and HIMU groups have combined $\mu^{142}Nd$ = -0.8 ±1.2 (MSWD: 0.6, probability of fit: 0.76, *n* = 7). Intensive measurement replication permits an overall uncertainty of less than 2 ppm for each sample group even with an estimated reproducibility of any single measurement of typically ca. 5 ppm (Supplementary Information). Further, the results represent data for replicate sample dissolutions processed through diverse chemical separation methods, thus improving their overall reliability (Supplementary Information). The EM group and the combined FOZO/HIMU groups pass a t-test for statistical distinctness (two-tailed P = 0.004). It is also notable that the two sample groups that represent recycled materials (HIMU, $\mu^{142}Nd$ = -0.7 ±1.4, and EM, $\mu^{142}Nd$ = +2.3 ±1.3) have statistically distinct $\mu^{142}Nd$ compositions, meaning that the geological evolution of these deep mantle components must have diverged in the Hadean Eon, and that LLSVP may contain materials with diverse Hadean histories. On the other hand, the Marquesas HIMU and FOZO groups have average $\mu^{142}Nd$ values that overlap within uncertainty, implying that their geological histories diverged only after the Hadean Eon.

Consistent with this inter-group heterogeneity, the $\mu^{142}Nd$ compositions of Marquesas lavas are correlated with their $^{87}Sr/^{86}Sr$ and $^{143}Nd/^{144}Nd$, and Ce/Pb ratios, and display a more complex, but interpretable relationship with their $^{206}Pb/^{204}Pb$ ratios (**Figures 3, S1**; Supplementary Information). This is the first time such a correlation between $\mu^{142}Nd$ and long-lived radiogenic isotopes or trace element ratios for geologically young rocks has been observed. There is no statistically significant correlation between $\mu^{142}Nd$ data and the siderophile W and Os isotopic systems (**Figure S1**, cf., [30]). The negative correlation between $\mu^{142}Nd$ and $\varepsilon^{143}Nd$ compositions requires that this relationship is not chronological, but instead reflects variable mixing of an EM-like component with high $^{87}Sr/^{86}Sr$, low $\varepsilon^{143}Nd$, and elevated $\mu^{142}Nd$ into the Marquesas mantle source.

The Hadean heritage of EM-type Marquesan lavas

The heterogeneous $\mu^{142}Nd$ signatures of the EM and FOZO/HIMU sample groups represent variable influence from at least one component that formed before the end of the Hadean Eon. This component was then subjected to later dilution with a mantle component possessing a $\mu^{142}Nd$ composition close to the presumed bulk Earth value ($\mu^{142}Nd \equiv 0$). The combined effect of this dilution on both $\mu^{142}Nd$ and the long-lived radiogenic isotope signatures of Marquesas lavas is most visible for the EM group of samples. The Marquesas EM group displays a maximum $^{87}Sr/^{86}Sr$ ratio of ca. 0.7054 and $\mu^{142}Nd$ up to +2.6 that trend toward the

isotopic composition of continental crust, which is inferred to be the source of subducted sediments that represent this EM endmember (e.g., Samoa, [34]). By contrast, the HIMU and FOZO groups have lower $^{87}Sr/^{86}Sr$ ratios and $\mu^{142}Nd$ very close to the bulk Earth (**Figures 3**, **S1**). The effect of diluting a FOZO-like component with an EM component on $\mu^{142}Nd$ can be predicted by calculating a Sr-^{143}Nd isotopic mixing line between idealized FOZO and EM components, and then projecting this line through the maximum $\mu^{142}Nd$ composition of the EM group and the average $\mu^{142}Nd$ composition of the Marquesas FOZO group ($\mu^{142}Nd = -1.0 \pm 2.2$). The Samoa hotspot, which overlaps and extends the Sr-Nd-Pb isotopic composition of Marquesas lavas toward an EM endmember composition (**Figures 1, S2**) can be utilized as an idealized EM endmember [34]. Due to the very radiogenic $^{87}Sr/^{86}Sr$ and unradiogenic $\varepsilon^{143}Nd$ signatures of Samoan lavas, the Samoa EM endmember has been interpreted to represent subducted sediments derived from felsic continental crust, which is the only material known to both share these isotopic properties and have trace element abundances high enough that these isotopic signatures can be recognized in derivative lavas [34]. Marquesas and Samoa OIB share a multi-dimensional isotopic composition [35], so the broad petrological and geochemical characteristics of their EM endmembers are likely equivalent. Importantly, however, the Marquesas EM component need not derive from exactly the same felsic sedimentary package as Samoa in order for them to approximately share an endmember Sr-^{143}Nd-Pb isotopic composition, which reflects primarily their felsic character (cf., [29]). Their respective EM endmember components may instead share a Sr-^{143}Nd-Pb isotopic composition while having distinct $\mu^{142}Nd$ signatures, as is common throughout the Archean record of felsic crust (e.g., [36]; see also Supplementary Information). Additionally, it is clear from the both the geochemical spectrum [37] and the geographical distribution [38] represented by EM-type hotspots that each hotspot likely represents a distinct recycled sedimentary package, which most likely represent distinct geochemical evolution pathways.

The compositional overlap between Marquesas and Samoa lavas is strong circumstantial evidence that they each have an endmember source component with an isotopic composition like that of recycled felsic continental crust. It is unlikely that the most extreme compositions of Marquesas lavas instead represent an endmember composition for several reasons. First, most felsic continental crust is Precambrian (>0.5 Ga old), and thus has Sr-^{143}Nd-Pb isotopic compositions that are more radiogenic than the most radiogenic Marquesas samples [39]. Second, if Marquesas samples with the most extreme Sr-^{143}Nd-Pb isotopic compositions were direct representatives of recycled crustal materials and, thus, represented an endmember composition, this would likely be expressed more clearly in their major and trace element

compositions. For example, they would likely be relatively silicic, display negative Nb anomalies and relative enrichments in U, Th, and Pb. These characteristics are not observed in any Marquesas lavas (e.g., [27]), but are observed in Samoan lavas that display isotopic compositions closer to their assumed EM endmember [34]. Finally, all Marquesas EM group samples have $^{3}He/^{4}He$ ratios close to MORB [40], whereas tectonically recycled materials are expected to have lower $^{3}He/^{4}He$ ratios because He is preferentially lost during subduction compared to U and Th, the radiogenic parents of ^{4}He (e.g., **Figure 1c-1d**; [41]). Thus, it is most likely that the Marquesas EM samples represent a relatively diluted EM endmember deriving from recycled felsic crust.

Utilizing the isotopic compositions of the most extreme EM sample of [34] (cf., [42]) and trace element abundances of Archean-aged crust compiled from the GEOROC database (Supplementary Information), the Marquesas EM group represents a ca. 0.6% contribution of a Samoan-like felsic EM endmember with $\mu^{142}Nd$ of $+24^{+10}_{-5}$ (**Figures 3, S3-S4**; see Supplementary Information for model details). Since Sr and Nd behave conservatively in modern sedimentary systems [43], it is reasonable that the trace element abundances of Archean-aged crust are close to those of Archean-aged subducting sediments. This mixing proportion compares favorably with the Marquesas EM mixing models of [28] and [30]. Importantly, many of the Archean rocks with the most positive $\mu^{142}Nd$ compositions are mafic, while the EM endmember implied by the Sr-^{143}Nd-Pb isotopic composition of Marquesas OIB is felsic. This difference between the maximum $\mu^{142}Nd$ compositions of mafic (+20) and felsic (+17) rocks is likely negligible, since these values are identical within long-term uncertainty of $\mu^{142}Nd$ analyses (ca. ±5 ppm). Nevertheless, we construct a secondary model representing the possibility that the recycled sediments in the Marquesas source represent mixed mafic and felsic progenitors. In a model calibrated to match the $^{87}Sr/^{86}Sr$, $\mu^{142}Nd$, and $\varepsilon^{143}Nd$ compositions of Marquesas OIB, the required $\mu^{142}Nd$ composition of the mafic sedimentary member is $+27^{+12}_{-7}$, identical, within uncertainty, to the result of the model for felsic sediments. This model additionally permits the bulk sedimentary package to possess a high proportion of mafic material (up to ca. 90%) while still matching the $^{87}Sr/^{86}Sr$ and $\varepsilon^{143}Nd$ compositions of Marquesas OIB. Given that felsic materials were likely initially scarce at Earth's surface, this result may present a more realistic view of the Hadean subduction environment that generated the Marquesas EM endmember while still requiring the presence of felsic materials on Earth at the time of this subduction.

Data for Earth's oldest rocks (up to 4 Ga old) approach this $\mu^{142}Nd$ compositions suggested by these mixing models, with a maximum recorded $\mu^{142}Nd$ value of +20 in a 3.85

Ga-old rock [44-47]. However, convective mixing quickly homogenized highly positive μ^{142}Nd signatures in Earth's mantle [48], such that the relative frequency of anomalous μ^{142}Nd signatures decreases rapidly through time (**Figure 4a-4b**) [49]. Preservation bias in the Archean rock record is unlikely to affect the modern perspective on this trend because lithologies that are relatively vulnerable to erosion, such as ultramafic rocks, do not systematically possess anomalous μ^{142}Nd values; instead, all lithologies with published μ^{142}Nd data have nearly identical μ^{142}Nd distributions (**Figure 4c**). Consequently, the probability that subducted felsic sediments possessed a μ^{142}Nd composition greater than +19 (i.e. the minimum permitted by Marquesas OIB data) decreases by almost 70% between 4.0 and 3.8 Ga (**Figure 4d**; Supplementary Material). However, since μ^{142}Nd values of +19 or higher are extremely rare, even in the oldest rock record, the calculated probability of subducting material with this μ^{142}Nd composition at any point in the Archean is very low (**Figure 4d**). Given the temporal trend of the μ^{142}Nd record toward more anomalous compositions in older rocks, the most probable way to generate recycled felsic sediments with μ^{142}Nd values greater than +19 is to generate them before 4 Ga, i.e. during the Hadean Eon. The subduction of sediments with highly anomalous μ^{142}Nd after this time cannot be completely excluded; for example, preferential erosion of small-mass Eoarchean terranes preserved in modern crust could generate sediments with anomalous μ^{142}Nd values if they remain undiluted by erosion of surrounding lithologies. However, such preferential erosion can be regarded as extremely unlikely, and the dominance of crustal rocks with μ^{142}Nd near zero in the Meso-Neoarchean record (**Figure 4b**) implies that generation of crustal sediments with μ^{142}Nd was similarly unlikely at that time. Consequently, the presence of sufficient felsic crustal material on Earth's surface by 4 Ga ago, as predicted by our simulation (**Figure 4**), supports both very early formation of felsic crust [5] and implies that tectonics in some form had been active for some time before 4 Ga.

A Hadean start for deep tectonic subduction

Our Nd isotopic data require that the Marquesas mantle plume taps a tectonically recycled component with a μ^{142}Nd signature at least as ancient as that found in Earth's oldest crustal rocks. This necessitates that tectonic subduction was not only active, but that subducted materials were transported deep enough into Earth's mantle that their compositions were preserved for billions of years, precluding models such as drip subduction, sagduction, or flat subduction (e.g., [50]). According to geodynamic models, the long-term preservation of heterogeneous isotopic domains in Earth's mantle is only likely in the deep mantle, and most probable within stable deep mantle structures [21]. This implies that the Hadean-aged

subduction that locked the μ^{142}Nd composition of the Marquesas EM endmember in the mantle was steep and did not result in stagnation of the subducting slab in the mantle transition zone, as envisaged by many models of ancient subducted crust [50, 51]. Since EM-like Sr-Nd-Pb isotopic compositions like those found in the Marquesas or Samoa are unknown among upper mantle-derived rocks [20], it is unlikely that the Marquesas mantle plume inherited its EM component from the upper mantle. Further, the strong preservation bias present in all materials from the early Earth implies that the Marquesas EM component is not unique: rather, it likely represents part of a larger recycled domain reflecting widespread Hadean subduction, only some of which survived to the present day.

Significantly, the operation of deep tectonic subduction by the end of the Hadean Eon strongly implies that the foundation for biogeochemical cycles critical for life was laid very early in Earth's history. Moreover, the subduction of sediments is often envisaged analogously to modern tectonic-erosional cycles and may require that continental erosion systems were also active on the early Earth (cf. the banded iron formation record, e.g., [52]). An early start to plate tectonics and a long evolutionary pathway to complex life on Earth places an important constraint on the search for Earth-like exoplanets as remote sensing and numerical simulation techniques improve. Given the long temporal gap between the emergence of terrestrial plate tectonics (≥4 Ga ago as proposed here) and the emergence of eukaryotic life (≥1.7 Ga [53]), young exoplanets without emerging plate tectonic processes may be much less likely to eventually host life. On the other hand, early development of plate tectonics is not a guarantee that a planet will eventually generate a biosphere [54, 55]. Additional high-precision study of the Hadean geochemical record preserved in subducted materials tapped by volcanic hotspots may provide a more detailed record of the early evolution of Earth's tectonic landscape. EM-type hotspots, in particular, are all geochemically unique, and the EM mantle component is increasingly recognized as representing diverse and independent geological heritages [39], some of which may have a geochemical history stretching back to the earliest Earth.

Acknowledgements

Funding for this project was provided by ETH Zürich/Marie Skłodowska-Curie Actions COFUND (18-1 FEL-28 to BJP) and the Swiss National Science Foundation (PZ00P2_180005 to BJP and project 200021_208079 to MS). The authors thank A. Giuliani and C. Walton for informative discussions and C. Maden for technical assistance with the TIMS.

Data availability statement

To facilitate review and ease of reader access, all data generated in this study are available in the Supplementary Tables. Additionally, these data will be archived in the EarthChem database and made public after manuscript acceptance.

Figures

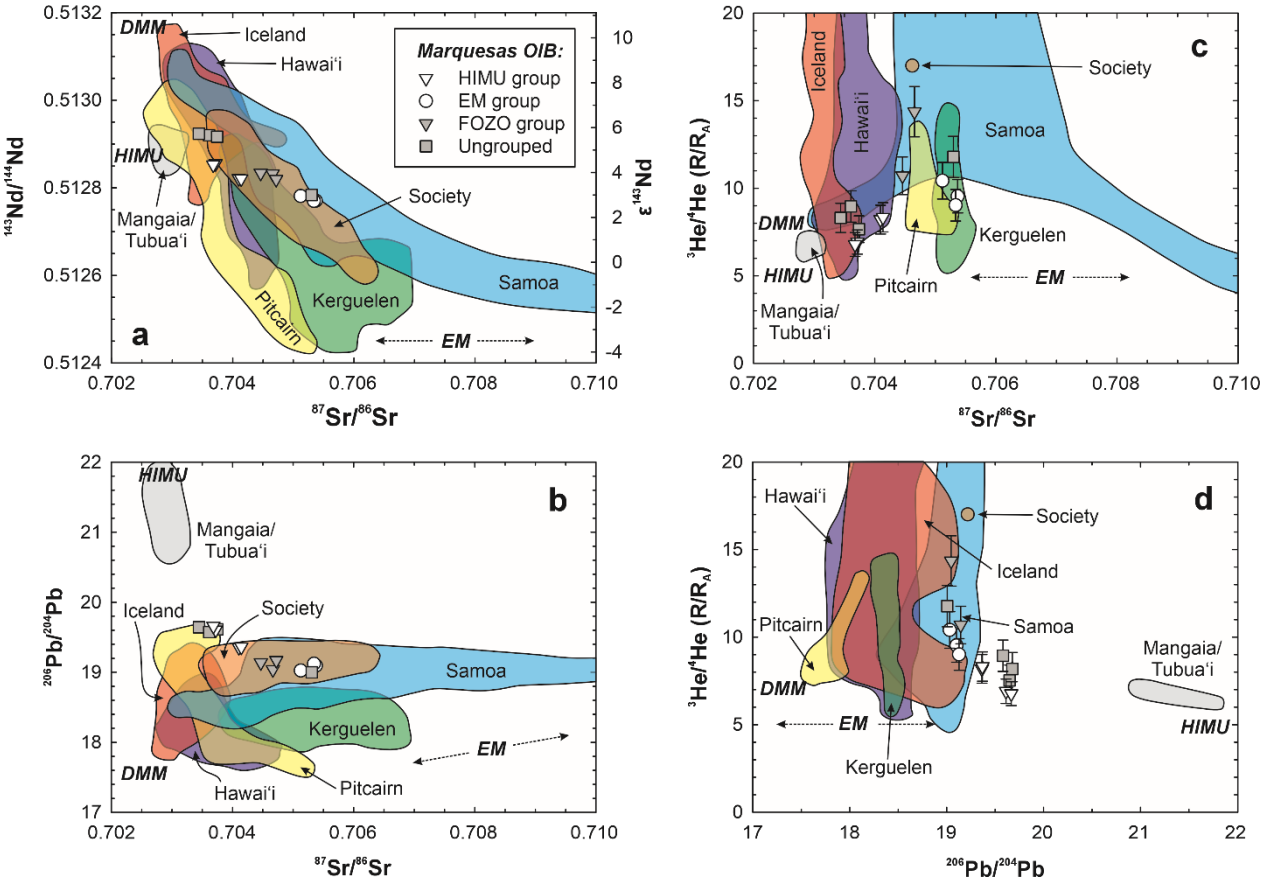

Figure 1. Isotopic compositions of Marquesas lavas (this study and Castillo et al., 2007; **Table S1**) compared with compositional ranges of global volcanic hotspots (data from GEOROC precompiled datasets, December 2023 versions). The approximate locations of recognized mantle components DMM (depleted mid-ocean ridge basalt mantle), HIMU (high-$^{238}U/^{204}Pb$ or high-μ), and EM (enriched mantle) are shown for reference. Neodymium isotopic compositions in ε notation are normalized to the chondritic uniform reservoir [56]; helium isotopic compositions are normalized to the $^{3}He/^{4}He$ ratio of air (R_A, 1.38 x 10^{-6} [57]). For a comparison of data for Marquesas lavas in this study and in the literature, see **Figure S2**.

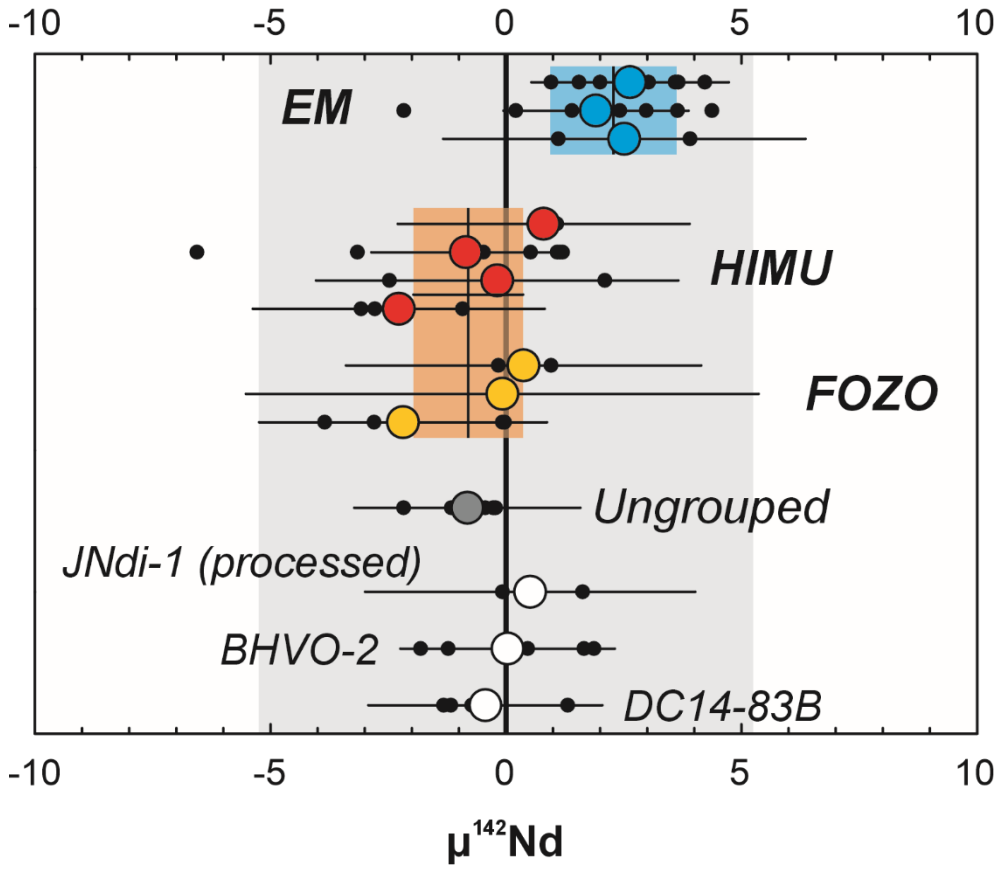

Figure 2. Neodymium-142 compositions of Marquesas lavas (normalized to the Nd standard JNdi-1, in parts per million), the Nd standard processed through separation chemistry, and reference materials (BHVO-2, DC14-83B). Black points show the results of individual measurements, colored symbols and error bars show the average and 95% confidence intervals of samples. Gray shaded region shows the average medium-term (1-2 years) 2σ standard deviation of Nd standard measurements. Colored shaded regions show the averages and 95% confidence intervals for sample groups determined by their long-lived radiogenic isotopic compositions (Supplementary Information).

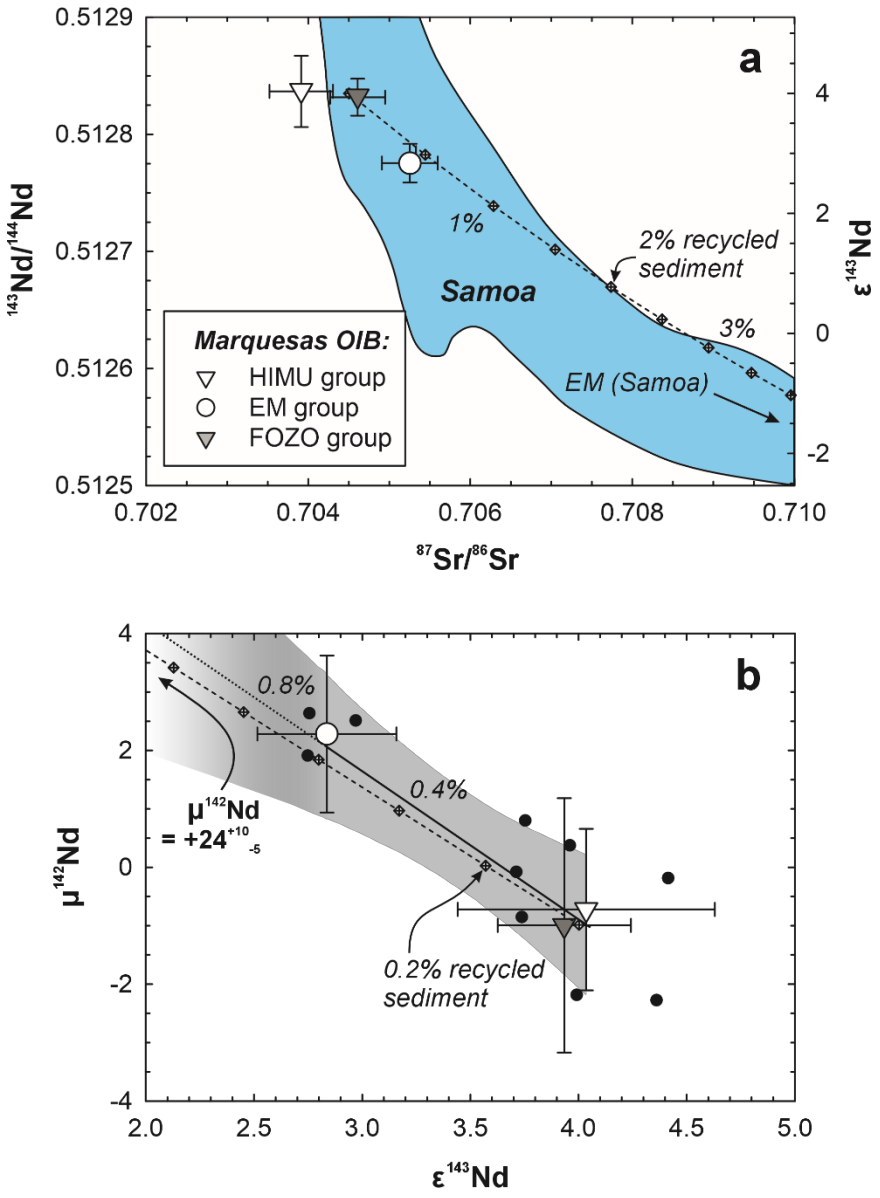

Figure 3. Mixing models (dashed lines) for the Sr-Nd isotopic compositions of Marquesas lavas assuming that the Sr-^{143}Nd isotopic composition of the EM endmember is compositionally similar to that of the Samoa hotspot ([34], cf., [42]). The solid black line and gray shaded region in (b) represent the York-type linear regression and 95% confidence interval, respectively, of the μ^{142}Nd-ε^{143}Nd data for Marquesas lavas [33]. The dotted black line and tapered gray shading represent an extrapolation of this regression. Large symbols and error bars show the per-group average and 95% confidence intervals, black circles show the per-sample compositions. The fraction of mixed EM component is noted by diamonds along the dashed mixing line. The compositional range of Samoa EM-type lavas is shown by the blue field (GEOROC database precompiled file, December 2023 version).

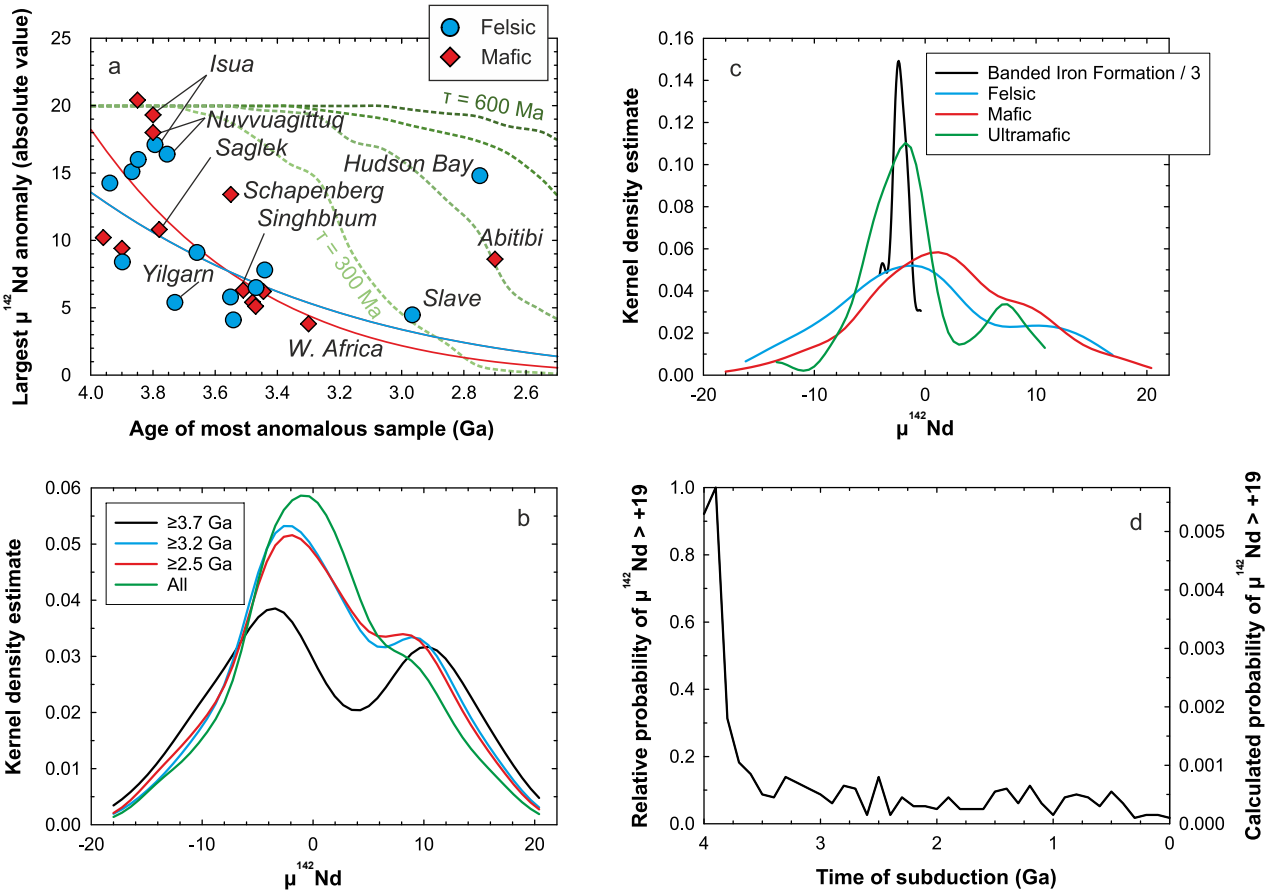

Figure 4. Temporal trends in μ^{142}Nd compositions. (a) Ages and largest μ^{142}Nd anomalies for well-studied Archean crustal localities, with regression curves for felsic and mafic samples (excluding Hudson Bay and Abitibi). Maximum μ^{142}Nd values predicted by the stirring models of [48] are shown for reference as dashed green lines with τ (stirring rates) of 300, 400, 500, and 600 Ma. (b) Kernel density estimates for global μ^{142}Nd data by age band, showing bimodal anomalous compositions largely disappearing by the end of the Eoarchean Era. (c) Kernel density estimates for global μ^{142}Nd data by lithology, showing that all major rock types integrated across all ages have averages near zero. Note that data for banded iron formations (*n* = 11, [58]) are relatively sparce compared to other lithological groups, leading to a sharper kernel density estimate peak. The secondary density peak for ultramafic rocks is comprised exclusively of rocks from the relatively densely sampled Saglek block [59] and may not be globally representative. No group shows a strong preference for μ^{142}Nd values above +19, as required by the mixing model (**Figure 3**), meaning that preferential erosion of any rock type will not strongly influence the composition of subducting material. (d) Bootstrap and Monte Carlo simulation of the probability that subducted sediments will possess an average μ^{142}Nd equal to or greater than +19 at any point in time, as required by the mixing model (**Figure 3**). Note that the absolute probabilities displayed on the right-side y-axis are arbitrary given the

setup of the simulation (Supplementary Materials), however they illustrate generally very low probabilities of subducting sediments with $\mu^{142}Nd \geq +19$ even at 4.0 Ga. Compiled data from [16, 19, 36, 44-47, 49, 58, 59] and additional references listed in the Supplementary Information.

Materials & methods and supplementary information for

Hadean-aged felsic sediments recycled through the deep mantle by early plate tectonics

Bradley J. Peters, Marc C. Halfar, Courtney J. Rundhaug, Paterno Castillo, Maria Schönbächler

Materials and Methods

Samples

Samples analyzed for their $^{142,143}Nd/^{144}Nd$ ratios were collected from the Marquesas Archipelago (South Pacific Ocean) by Harmon Craig (formerly Scripps Institution of Oceanography) and comprise eight samples from the island of Hiva Oa, two from Fatu Hiva, and one from Nuku Hiva. The Marquesas Islands display geographically age-progressive eruption chronology: the oldest lavas were erupted at the northwestern end of the archipelago (Eiao Island) ca. 5 Ma ago, and the youngest known lavas were erupted at its southeastern side (Fatu Hiva) ca. 1 Ma ago [60]. The archipelago overlies the Pacific large low shear wave velocity zone (LLSVP) and is fueled by a mantle plume that can be imaged by seismic tomography through at least half of Earth's mantle [22]. It is also likely underlain by an ultra-low velocity zone (ULVZ), which contains dense, likely Fe-rich material [61]. For these reasons, the Marquesas hotspot is typically considered to be one of Earth's primary hotspots that taps deep mantle reservoirs observed in its geochemical compositions.

Except for sample HO-AT-Gabbro, the samples considered in this study, along with additional samples from Fatu Hiva and Nuku Hiva, were studied by [40] (He-Sr-^{143}Nd-Pb isotopic compositions) and [28] (^{187}Os isotopic compositions and highly siderophile element abundances). A subset of the samples considered here were studied in [30] (Nd and W isotopic compositions). The sample powders used in this study are aliquots of those used in [40] and the Sr-^{143}Nd-Pb isotopic compositions of these samples determined in this study are consistent with what was reported in [40] (**Table S1**). The Nd isotopic data presented in this manuscript is expanded from those reported in [30] and includes new Sr-^{142,143}Nd-Pb isotopic analyses. The samples in this study are alkali basalts (SiO_2 = 45.0 – 48.3 wt.%, $Na_2O + K_2O$ = 2.3 – 5.3 wt.% across all samples). Because the samples were originally intended for study of noble gases, they are exclusively fresh, olivine-phyric and represent surficial flows primarily from the post-shield stage of the islands.

The Sr-^{143}Nd-Pb isotopic compositions of the samples in this study overlap those of literature data for the Marquesas Islands and mirror their trends (**Figure S2**) but do not capture some of the highest $^{87}Sr/^{86}Sr$ ratios (up to 0.7065, this study up to 0.7054) and lowest $\varepsilon^{143}Nd$ compositions (down to +1.2, this study down to +2.6) recorded in some published data (e.g., [27, 62-64]). Together, the published and new Sr-^{143}Nd isotopic compositions define a trend roughly connecting a moderately depleted composition (similar to HIMU or the mantle focal zone, FOZO, also known as C, common component, and PREMA, prevalent mantle; e.g., [65]) to an enriched composition, paralleling the trend of Samoa OIB towards an enriched mantle 2

(EM2)-like endmember (**Figure 1**; cf., [34]). A subset of samples, primarily from the island Fatu Hiva, trend toward radiogenic Pb isotopic compositions in the direction of HIMU (e.g., Mangaia; [66]). It is notable that, regardless of their He-Sr-^{143}Nd-Pb isotopic compositions, all of these samples display nearly constant and relatively unradiogenic $^{187}Os/^{188}Os$ ratios [28]. These authors interpreted this signature as reflecting a dominant role for Os-rich peridotite lithologies in the overall Os budget of Marquesas lavas, and a relatively unimportant role for Os-poor and incompatible-rich source components like EM. Since the Os isotopic compositions of Marquesas lavas do not participate in the mixing trends that are clear in the Nd isotopic data, they are not considered in the sample grouping process or the interpretation of μ^{142}Nd data using these mixing trends.

There is also significant variability in $^{3}He/^{4}He$ ratios among Marquesas lavas [40]. Samples from Fatu Hiva have MORB-like (8 ±2 R_A; [57]) to low $^{3}He/^{4}He$ ratios (to 6.8 R_A), a characteristic again associated with HIMU-type OIB. By contrast, samples from Hiva Oa show MORB-like to elevated $^{3}He/^{4}He$ ratios (to 14.4 R_A). Elevated $^{3}He/^{4}He$ ratios are commonly associated with moderately depleted Sr-^{143}Nd-Pb isotopic compositions that are similar to the global FOZO component. Among Marquesas lavas, the highest $^{3}He/^{4}He$ ratios are associated with moderately depleted ε^{143}Nd values around +4. However, one sample (HO-AT-3) with elevated $^{87}Sr/^{86}Sr$ ratios and lower ε^{143}Nd compositions that trend toward an EM endmember also possesses a $^{3}He/^{4}He$ ratio greater than the MORB range.

These isotopic characteristics permit the division of the samples into groups that are most characteristic of the FOZO, HIMU, and EM mantle components. In the EM group are two samples from the Puamau Bay area of Hiva Oa (HO-PUA-2 and HO-PUA-3) that strongly overlap with the Ua Huka group of [27] (**Figure S2**), along with other young Hiva Oa samples that are characteristic of the Puamau Bay area. The third member of the EM group is sample HO-AT-4, which was collected in the center of Hiva Oa and also strongly overlaps with the Ua Huka group. This group has high $^{87}Sr/^{86}Sr$ ratios (>0.7051), low ε^{143}Nd values (<3.0), and $^{3}He/^{4}He$ ratios overlapping with the upper range of MORB. The HIMU group is composed of two samples from the Hanaiapa Bay area of Hiva Oa (HO-HI-2 and HO-HI-3) and two samples from Fatu Hiva (FH-OM-3 and FH-TOP), all of which strongly overlap the Fatu Hiva group of [27] (**Figure S2**) for their $^{87}Sr/^{86}Sr$, $^{143}Nd/^{144}Nd$, and $^{206}Pb/^{204}Pb$ isotopic compositions. The samples from Hiva Oa have $^{206}Pb/^{204}Pb$ ratios greater than 19.35, and those from Fatu Hiva have $^{206}Pb/^{204}Pb$ ratios greater than 19.60. The FOZO group is comprised of two samples from the village of Atuona on Hiva Oa (HO-AT-1 and HO-AT-Gabbro) and the single sample from Nuku Hiva (NH-HA-1). Like other samples from these localities, they strongly overlap with

the Ua Huka group of [27] (**Figure S2**) and have lower $^{206}Pb/^{204}Pb$ ratios (< 19.2) than Hiva Oa samples with HIMU affinity. Sample HO-AT-1 additionally has a $^{3}He/^{4}He$ ratio (14.4 ±1.4 R_A) that is statistically higher than MORB. It is notable that both samples from the FOZO and EM groups strongly overlap with the Ua Huka group trends of [27] whereas the HIMU group overlaps the Fatu Hiva group trends (**Figure S2**). However, together these samples define a single sublinear trend in He-Sr-^{143}Nd-Pb isotopic diagrams that transverses the Fatu Hiva and Ua Huka trends; thus, we find it more straightforward to interpret the samples in terms of commonly used isotopic components (FOZO, EM, and HIMU) rather than utilizing the Fatu Hiva and Ua Huka trends. This choice does not contradict the existence of these isotopic "stripes" [27]. Instead, it merely parameterizes their componentry using well-studied mantle components rather than the more sophisticated componentry analysis of [27]. In this sense, the effect of the grouping on $\mu^{142}Nd$, which we later discuss in terms of a stronger (EM group) versus weaker (FOZO + HIMU) EM components could instead be reframed as a stronger versus weaker B or D component in their terminology, where both B and D both trend toward an EM2- or Samoa-like component. The FOZO group would then be described as having a stronger A component along the Ua Huka trends, which [27] interpreted as being intrinsic to the Marquesas plume, and the HIMU group possesses a stronger C component (not to be confused with the C or FOZO component) along the Fatu Hiva trends. Some Ua Huka trends imply that the A component of [27] may is relatively ^{206}Pb-rich. However, such a trend is not visible in our data that otherwise have Sr-^{143}Nd-^{206}Pb isotopic compositions that overlap the Ua Huka trends (**Figure S2**).

There are four samples from [40] that do not easily fit into the FOZO, EM, or HIMU isotopic groups. Three of these samples are from Fatu Hiva (FH-HV-2, FH-HV-3, FH-OM-1), and have elevated $^{206}Pb/^{204}Pb$ (>19.5) ratios, which are characteristic of the HIMU group. However, they have generally lower $^{87}Sr/^{86}Sr$ ratios (<0.7038) and substantially higher $\varepsilon^{143}Nd$ values (> +5.6) than the HIMU group, which places these samples closer to the Ua Huka trends of [27] (**Figure S2**), rather than the Fatu Hiva trends that are associated with most HIMU-type Marquesas lavas. Sample HO-AT-3 was collected from the same locality as sample HO-AT-1 (FOZO group), and it likewise has a $^{3}He/^{4}He$ ratio (11.8 ±1.4 R_A) that is statistically higher than MORB. However, unlike the FOZO group samples, HO-AT-3 has an elevated $^{87}Sr/^{86}Sr$ ratio (0.705306 ±0.000006) and a lower $\varepsilon^{143}Nd$ composition ($\varepsilon^{143}Nd \approx +3$), which are intermediate to the compositions of the EM and FOZO groups. Of the four ungrouped samples, this was the only one measured for its $\mu^{142}Nd$ composition, which strongly overlaps with the combined FOZO and HIMU group average (**Table S1**). However, due to the ambiguous long-lived

isotopic signature of this sample, its $\mu^{142}Nd$ composition is excluded from interpretation (see also later discussion of statistical treatment of sample grouping).

Sample dissolution and general sample treatment

Samples digested for Sr and Pb isotopic measurements, but not reference materials, were leached in 2M HCl at 60°C for about one hour prior to digestion. Samples digested for Nd isotopic measurements were not leached, following the methods of previous ^{142}Nd studies (e.g., [16, 67]). All samples were dissolved in a mixture of 4:1 ultrapure HF and double-distilled HNO_3 in 15 mL Savillex Teflon jars on a Teflon-coated hotplate at 140°C. Typically, complete dissolution was achieved in 1-3 days; in some cases, refractory dark grains remained, and in these cases the dissolution step was repeated. Samples were then taken up in solutions of 6-8M HCl and refluxed for 1-2 days on a Teflon-coated hotplate at 120°C. In most cases, this step was sufficient to break up residual solid flourides and produce transparent sample solutions, however in some cases this step had to be repeated one or more times to obtain transparent solutions. All chemical procedures described below utilized ultrapure (H_2O, HF, H_3PO_4) or double-distilled (HCl, HNO_3) reagents and precleaned Teflon sample containers.

Neodymium separation and Nd isotopic measurements

Neodymium was separated from matrix elements and other rare earth elements (REE, especially Ce and Sm) using methods modified from [67-69]. In the first method (cf., [67]), matrix separation was achieved using Bio-Rad AG® 50W-X8, 200-400 mesh cation resin, and Ce separation was achieved by oxidizing the sample with $NaBrO_3$ and then separating Ce with Eichrom LN resin (50-100 μm). Residual Na from the $NaBrO_3$ was separated again using Bio-Rad 50W-X8 cation resin (200-400 mesh), then Nd was separated from remaining REE on a 6 mm inner diameter x 12 cm length Teflon column filled with Eichrom LN resin (20-50 μm). In the second method (cf., [69]), matrix separation again used Bio-Rad AG® 50W-X8, 200-400 mesh cation resin. For Ce and Sm separation, a column containing Eichrom DGA resin (normal/unbranched, 50-100 μm) was positioned directly under a column containing LN resin in a "tandem" configuration. The sample was oxidized with $NaBrO_3$ and passed onto the upper LN column. The eluate from this column was allowed to drip directly onto the DGA column, where residual Na was then removed using additional 3M HNO_3. Following this, Nd was separated from other REE using 0.5-2.5M HCl solutions. Yields for the first method were typically 70-90% and yields for the second method were typically 80-95%; in both cases, most Nd was lost during the procedures utilizing cation resin. For this reason, the second method was

again modified so that matrix separation was instead accomplished using DGA resin (normal/unbranched, 50-100 μm; cf., [68]), and a third step utilizing a long-aspect (6 mm ID x 6 cm length) Teflon column filled with DGA resin (normal/unbranched, 50-100 μm) was added. In all cases, these methods typically resulted in measured $^{140}Ce/^{144}Nd$ and $^{147}Sm/^{144}Nd$ ratios that were similar to the JNdi standard. However, the third method utilizing the long-aspect DGA column also produced $^{141}Pr/^{144}Nd$ ratios that were typically <1 x 10^{-4}, whereas the first two methods typically produced measured $^{141}Pr/^{144}Nd$ ratios that were between 5 x 10^{-2} and 1 (i.e., 2-4 orders of magnitude higher).

For each method, the effects of the separation chemistry on isotopic compositions were monitored by repeated separations and measurements of the BHVO-2 reference material and by processing the JNdi standard through the chemistry procedure (**Figure S5**). In the case of BHVO-2, a separation utilizing the first method yielded $\mu^{142}Nd$ = +1.7 ±5.4 (2σ standard deviations, s.d., external, *n* = 1; see below for an explanation of precision reporting), separations utilizing the second method yielded $\mu^{142}Nd$ = +0.1 ±2.9 (95% c.i., MSWD = 0.2, *n* = 4), and a separation utilizing the third method yielded $\mu^{142}Nd$ = -1.8 ±5.2 (2σ s.d. external, *n* = 1). Together, these analyses yielded an overall average for BHVO-2 of $\mu^{142}Nd$ = 0.0 ±2.3 (95% c.i., MSWD = 0.3, *n* = 6) and $\varepsilon^{143}Nd_{CHUR}$ = +6.73 ±0.018 (95% c.i., MSWD = 0.8, *n* = 5), the latter of which agrees with the preferred GeoREM [70] value of +6.8 ±0.5. In the case of JNdi processed through separation chemistry, the first method yielded $\mu^{142}Nd$ = +1.6 ±6.6 (2σ s.d. external, *n* = 1), the second method yielded $\mu^{142}Nd$ = +0.3 ±6.8 (2σ s.d. external, *n* = 1), and the third method yielded $\mu^{142}Nd$ = -0.1 ±5.2 (2σ s.d. external, *n* = 1) for overall averages of $\mu^{142}Nd$ = +0.5 ±3.5 (95% c.i., MSWD = 0.1, *n* = 3) and $\varepsilon^{143}Nd_{CHUR}$ = -10.27 ±0.03 (95% c.i., MSWD = 2.7, *n* = 3). An in-house standard, DC14-83B (a lamprophyre from the Deccan Traps) was additionally processed through the first (*n = 3*) and second (*n* = 2) separation methods and yielded an overall average $\mu^{142}Nd$ = -0.4 ±2.5 (95% c.i., MSWD = 0.2, *n* = 5) and $\varepsilon^{143}Nd$ = -1.50 ±0.04 (95% c.i., MSWD = 2.5, *n* = 5) with no significant difference between the separation methods (**Figure S5**). For all three materials, separation methods 2 and 3 yield $\varepsilon^{143}Nd$ compositions slightly higher than, but within analytical uncertainty of, the $\varepsilon^{143}Nd$ compositions produced from separation method 1. Such differences in Nd isotopic compositions may be generated by mass-dependent effects arising from the behavior of Nd on separation resins, however for the observed difference of <6 ppm, the corresponding effect on measured $^{150}Nd/^{144}Nd$ ratios would be ca. -50 ppm (cf., [67]), which is greater than analytical uncertainty and not observed in the data. Further, the observed offsets are less than analytical uncertainty for the respective measurements (**Figure S5** and **Tables S2** and **S3**). It is thus evaluated that

there are no meaningful differences in data generated for samples processed through the different separation methods and no differences attributable to mass-dependent fractionation effects arising during resin-assisted chemical separation. The strong agreement between measured Nd isotopic compositions of samples processed through different chemical separation methods also attests to their robustness (**Tables S2** and **S3**).

Residual effects from the chemical separation were also tested observationally. There is no correlation between the total procedural yield of BHVO-2 and any measured Nd isotopic composition that is resolvable outside of analytical error (**Figure S6**). One BHVO-2 replicate with a yield of ca. 79% has coincident negative μ^{148}Nd and μ^{150}Nd, neither of which are resolvable from 0 given the medium-term or 2σ s.d. of JNdi-1 standards run in the same session. Coincident negative μ^{148}Nd and μ^{150}Nd signatures are an expected result of mass-dependent fractionation effects arising from LN-resin, although it is expected only at very low yields [67, 71]. However, this effect would also be expected to produce positive offsets in ε^{143}Nd [67], whereas this sample has a ε^{143}Nd composition that is indistinguishable from samples that have μ^{148}Nd and μ^{150}Nd signatures very close to zero (**Table S3**). The effects of mass-dependent effects arising from chemistry on μ^{142}Nd are proportionally much smaller in magnitude than the effects on μ^{148}Nd and μ^{150}Nd, and this sample shows no statistically resolvable difference in μ^{142}Nd compared to other measurements of BHVO-2 (**Table S3**). It is therefore assessed that coincident ^{148}Nd and ^{150}Nd deficits up to the magnitude observed in this measurement (μ^{148}Nd = -12.3 ±10.8 and μ^{150}Nd = -39 ±35) are unlikely to affect μ^{142}Nd or ε^{143}Nd; in any case, deficits of this magnitude are never observed in our sample data.

Cerium and Sm doping tests were also performed to test the effectiveness of interference corrections on ^{142}Nd/^{144}Nd and ^{143}Nd/^{144}Nd ratios (**Figure S7**). In all cases, JNdi-1 standards doped with Ce or Sm yielded Nd isotopic ratios that were within the medium-term and session 2σ standard deviation for all undoped and unprocessed JNdi-1 standards. However, some possible trends may be observed. For all measured ^{140}Ce/^{144}Nd ratios ($<7 \times 10^{-4}$), the measured ^{142}Nd/^{144}Nd ratios are within 3 ppm of the average of all undoped standards measured in that session. However, JNdi-1 standards with higher ^{147}Sm/^{144}Nd also display progressively higher ^{142}Nd/^{144}Nd and ^{143}Nd/^{144}Nd ratios. These correlations imply that the Sm interference correction for ^{144}Nd begins to fail at relatively low levels of Sm, perhaps for ^{147}Sm/^{144}Nd $> 1 \times 10^{-5}$, and that the assumed ^{144}Sm/^{147}Sm ratio used for this correction (0.205034) results in a slight overcorrection and thus slightly higher ^{142,143}Nd/^{144}Nd ratios. Notwithstanding, there is no correlation between measured ^{147}Sm/^{144}Nd and ^{145}Nd/^{144}Nd, ^{148}Nd/^{144}Nd, or ^{150}Nd/^{144}Nd ratios (the latter two of which are most strongly affected by Sm interferences), and it is again

emphasized that in all cases the measured $^{142}Nd/^{144}Nd$ and $^{143}Nd/^{144}Nd$ ratios of Sm-doped standards were within the 2σ s.d. of the undoped standards in the same session, implying that this observed correlation may be erroneous. Throughout this study, no measured sample possessed a measured $^{147}Sm/^{144}Nd$ ratio greater than the minimum threshold value of 1×10^{-5} nor a measured $^{140}Ce/^{144}Nd$ ratio greater than the minimum threshold value of 7×10^{-4} evaluated in these doping tests. Thus, neither Ce nor Sm interferences impact our data in a meaningful way.

Total procedural blanks (TPB) were monitored periodically throughout the study. These yielded Nd blanks of 12-29 pg (n = 3). Wash eluates were also regularly monitored from the DGA resin, since it is known to have a significant Nd memory effect [68], and these contained up to ca. 200 pg Nd. The tests document the effectiveness of our cleaning method, but nevertheless raise the concern that some of this Nd could be released into sample solutions without detection in our TPB analyses. Thus, these tests were used to determine the maximum number of times the DGA resin was reused before being discarded: for the primary matrix separation, Ce separation, and La-Pr separation on the long aspect columns, the resin was used a maximum of 3, 5, and 7 times respectively. Sample HO-AT-Gabbro contained the least processed Nd at ca. 200 ng, such that in the worst case the wash blank would represent up to 0.1% of processed Nd. The remainder of the samples have high Nd abundances (>20 ppm), such that a more typical blank (based on the TPB) would represent <0.002% of the Nd processed through chemistry. Thus, blanks do not affect measured Nd isotopic compositions and no blank corrections are performed on the data.

Isotopic measurements were carried out using the Thermo Scientific Triton thermal ionization mass spectrometer (TIMS) in the Isotope Geochemistry and Cosmochemistry group, Institute of Geochemistry and Petrology, ETH Zürich. Before sample loading, 0.3 µL of 0.1M H_3PO_4 was evaporated to near dryness on 99.99-99.999% purity Re filament. Samples were dissolved in 2M HCl and loaded directly onto the residual liquid H_3PO_4 in aliquots of ~0.2 µL. Between each aliquot loading, the liquid was partially dried under a current of 0.7-1.0 A, and this typically resulted in final spot sizes of 0.5-1.5 mm. Measurements utilized nine Faraday cups in a 1 amu spacing configuration and equipped with 10^{11} Ω amplifiers (cf., [67]). The measurement was performed in cycles of four lines each, with masses 143, 144, 145, and 146 sequentially directed into the center cup. This results in two dynamic $^{142}Nd/^{144}Nd$, $^{143}Nd/^{144}Nd$, and $^{148}Nd/^{144}Nd$ ratios, three dynamic $^{145}Nd/^{144}Nd$ ratios, and one static $^{150}Nd/^{144}Nd$ ratio per cycle. Measurements were done without amplifier rotation, and amplifier gain analyses were either performed before each sample (once) or before each measurement session (average of 8-

10 separate gain calibrations); both strategies revealed <5 ppm, and often <3 ppm, variability in gain factors across single sessions. A typical measurement consisted of 600 cycles and lasted about 10 hours.

Measured Nd isotopic ratios were normalized to a $^{146}Nd/^{144}Nd$ ratio of 0.7219 using the exponential law (cf., [67]). A time correction was applied to calculate the $^{146}Nd/^{144}Nd$ ratio measured at the same time as the Nd isotopic ratios of interest; for example, to calculate the lines 1-3 dynamic $^{142}Nd/^{144}Nd$ ratio, the static $^{142}Nd/^{144}Nd$ ratio from line 1 is used and a regression of $^{146}Nd/^{144}Nd$ ratios from line 3 versus time (moving window of ±5 cycles) was used to determine the $^{146}Nd/^{144}Nd$ ratio that would be measured in the line 3 configuration at the time when the line 1 $^{142}Nd/^{144}Nd$ ratio is integrated (see [67] for further discussion). Runs were further monitored for positive linear increases in $^{146}Nd/^{144}Nd$ ratios because deviations from positive linear behavior can indicate that distinct domains are simultaneously ionizing on the filament, which can lead to non-exponential fractionation of Nd isotopes [72]. Whenever non-linear, negatively sloped, or relatively rapid fractionation of $^{146}Nd/^{144}Nd$ ratios was observed, the corrected data were manually examined in sections. Anomalous run sections with non-linear $^{146}Nd/^{144}Nd$ fractionation were compared to a preferred section from the same run that displayed the most prolonged positive, linear $^{146}Nd/^{144}Nd$ fractionation for that run. If any of the average dynamic $^{142,143,145,148}Nd/^{144}Nd$ ratios for the anomalous section were statistically resolved from (utilizing the 2σ s.e. of each respective run section) the preferred section, or the corrected $^{142}Nd/^{144}Nd$ ratios deviated from exponential-law behavior by more than 30 ppm in the anomalous section, the anomalous section was removed from the data reduction. An example of this filtering method applied to replicate runs of the same sample is shown in **Figure S8**. Anomalous $^{146}Nd/^{144}Nd$ fractionation requiring data filtering of any degree affected approximately one in five runs. After data filtering, the affected runs always returned dynamic $^{142,143}Nd/^{144}Nd$ ratios within uncertainty of the same ratios for replicate runs of the same sample that did not display anomalous $^{146}Nd/^{144}Nd$ fractionation. If there was no prolonged period of positive, linear $^{146}Nd/^{144}Nd$ fractionation in a run, the entire run was rejected. Independent of fractionation behavior, if the averages of either dynamic $^{142}Nd/^{144}Nd$ ratio did not converge by the end of the run i.e., they displayed continuously increasing or decreasing behavior, or oscillating behavior throughout the run, the entire run was rejected. If the combined whole-run average of static lines 1-2 $^{142}Nd/^{144}Nd$ ratios, which are respectively used to calculate the dynamic lines 1-3 and 2-4 $^{142}Nd/^{144}Nd$ ratios, deviated from exponential-law behavior by more than 5 ppm, the entire run was rejected. Less than 5% of all runs were rejected using these criteria.

The ability of our analytical setup to produce Nd isotopic data consistent with those previously obtained at Carnegie Institution for Science [73, 74] was evaluated by re-measuring samples with heterogeneous μ^{142}Nd values. A subset of these replicate results was already published and demonstrates strong consistency between the analytical setups at ETH and Carnegie [74]. We further re-measured the compositions of Réunion hotspot lava samples RU0709 and RU0711, which displayed the largest-magnitude positive and negative μ^{142}Nd compositions, respectively, from replicate measurements undertaken at Carnegie [73]. Our new results are statistically consistent with the previous results (**Table S2**). However, they display somewhat less extreme μ^{142}Nd compositions than those previously reported [75]. Including the new results and recalculating replicate statistics as described below, the average μ^{142}Nd composition for RU0709 is +5.5 ±2.5 (MSWD = 0.7) and for RU0711 is -7.2 ±2.7 (MSWD = 0.5), thus confirming the presence of strongly heterogeneous μ^{142}Nd signatures in the Réunion hotspot mantle source.

Data statistics and reporting for Nd isotopic compositions

The external precision for each measurement was estimated as the largest of (1) the 2σ s.e. of all cycles in an individual measurement (typically ca. 2 ppm for dynamic ^{142}Nd/^{144}Nd ratios), (2) the 2σ s.d. of all JNdi-1 standards run in the same barrel as the sample (1.3-6.8 ppm), or (3) the medium-term precision (5.2-6.9 ppm). The medium-term precision is estimated as the 2σ s.d. of all JNdi-1 standards run by all instrument users in all barrels over the course of this study, with a correction applied for observed data trends related to the gradual degradation of Faraday cup liners (cf., [67]). The medium-term precision calculation was then reset whenever the Faraday cup liners are replaced; during the course of this study, they were replaced in August 2020 and May 2023, meaning that a total of three sets of cup liners were utilized during this study. Medium-term precisions are summarized in **Table S4**. This approach to data precision reporting has several advantages. It permits capturing of instrument or measurement instabilities over short (precision measure 1), medium (precision measure 2), and long (precision measure 3) timescales. For example, the true reproducibility of a single poor-quality measurement within a barrel with generally good-quality measurements will be more accurately captured by the 2σ s.e. of all cycles in an individual measurement (precision measure 1). In comparison, the reproducibility of a good-quality sample measurement within a barrel with many poor-quality measurements will be captured by the 2σ s.d. of multiple standard measurements (precision measure 2), which may capture weeks-scale instrument instabilities not reflected by the 2σ standard error of sample measurements (i.e. 2 σ s.e.m.; individual

measurements are ca. 12 hours long). Long-term instrumental instabilities, including amplifier drift or instability, degradation of internal electrical parts, or inaccurate gain or baseline calibrations can be effectively captured by medium-term reproducibility of JNdi standards (precision measure 3).

In practice, the medium-term reproducibility of JNdi standards (precision measure 3) is almost always the largest and therefore the most conservative value. However, its application is statistically justified in hindsight: the typical approach of estimating single-measurement precision using the 2σ s.e.m. alone shows that repeated measurements and repeated digestions are sometimes statistically distinct (i.e. their values do not overlap within 2σ s.e.m. precision), implying that this estimate of measurement uncertainty underestimates the true measurement uncertainty. This can be illustrated, for example, using the Isoplot probability of fit and Model-2 functions (in IsoplotR, this is known as the "random effects model"). Probability of fit calculates the chance that the data uncertainty represent a "true" data array with the same amount of dispersion (according to the composition assigned to each sample) or less. A low probability of fit thus implies that a sample group represents a true data distribution that is more dispersed than the assigned compositions alone, while a high probability of fit implies that the sample group is less dispersed than the assigned compositions. In the case of two measurements that are distinct or nearly distinct considering their respective 2σ s.e.m., but not distinct considering the 2σ s.d. of all standards measured in the same respective barrels, Isoplot will return low probabilities of fit if the input errors reflect the 2σ s.e.m. and higher probabilities of fit for input errors that reflect the 2σ s.d. of all standards from the same barrel. In the former case, the strict statistical interpretation of this result is that the measurements represent two separate sample populations, something that is not expected within single samples for an element like Nd, which is not known to suffer from nuggeting effects. On the other hand, applying uncertainty estimates as described here often results in per-sample MSWD less than 1 (**Table S3**), which indicates a possible overestimation of sample uncertainty. We assess that, in the absence of knowing the true uncertainty of any given sample estimate, overestimation of sample uncertainty (thus producing MSWD <1 and larger 95% confidence intervals for replicate sample measurements) is geologically preferrable to underestimation of sample uncertainty, which may lead to the inference of heterogeneous isotopic compositions where in reality none exist.

For multiple measurements of the same sample that are statistically distinct from each other when considering their respective 2σ s.e.m., Isoplot suggests a Model-2 fit, where it predicts the existence of an unknown, external source of error and estimates its magnitude. In

many cases, Isoplot calculates the magnitude of this error source to be similar to the estimated medium-term precision, which is larger than measurement 2σ s.e.m.. This provides circumstantial evidence that this is a closer estimate of the true per-measurement precision than 2σ s.e.m. alone. A comparison of replicate sample statistics using the uncertainty determination described here versus the more typical practice of using 2σ s.e.m. alone is provided in **Table S5**.

It is important to acknowledge that expected μ^{142}Nd heterogeneity in modern, mantle-derived rocks is barely larger than analytical precision, although multiple independent studies have verified its existence [16, 48, 73]. Statistically resolving small-scale geochemical heterogeneity is challenging, particularly if the magnitude of medium-term precision is greater than the magnitude of expected sample heterogeneity. This study therefore uses sample replication as a strategy to precisely determine the μ^{142}Nd compositions of samples. Sample replication is very time intensive with TIMS analyses, because a single sample digestion may only provide enough Nd for 1-2 measurements, and each measurement duration is ca. 12 hours. Notwithstanding, sample replication is crucial to assess the effect of potentially overestimated or erroneous precision during hypothesis testing. In this context, repeated measurements of samples, which each provide an independent estimate of the effect of random analytical noise and the effects of sample handling that cannot be unambiguously quantified (e.g., filament loading technique), limits the impact of measurement error on overall sample results. However, sample replication cannot infinitely reduce inferred uncertainty on a per-sample basis. For example, assuming that medium-term precision drives the assigned per-sample uncertainty (see discussion above), a numerical simulation yields a typical 95% confidence interval after two sample measurements between ca. 3.5-4 ppm, if the medium-term precision is ca. 5.4 ppm (equal to that for the Faraday cup liners used over most of this study). After five measurements, the 95% confidence interval decreases to ca. 2-3 ppm and approaches a theoretical limit equal to the 2-standard error (s.e.) of replicate measurements. Improved per-sample precision also improves the minimum theoretical 95% confidence interval of sample replicates; for example, a per-sample precision of 3 ppm produces 95% confidence intervals of ca. 1.2-2.2 ppm for $n \geq 5$ and a per-sample precision of 2 ppm produces 95% confidence intervals of ca. 0.9-1.7 ppm for $n \geq 5$. Note, however, that a per-sample precision of 2 ppm requires that the medium-term precision, per-barrel 2σ standard deviation of standards, and per-sample internal precision all remain at or below 2 ppm over the temporal course of sample replication.

Layered on top of analytical error is additional randomness introduced by geological processes that cannot be realistically quantified on a per-sample basis. For example, samples

deriving from the same batch of magma ought to theoretically possess identical μ^{142}Nd compositions that reflect the μ^{142}Nd compositions of their mixed mantle sources, but in practice data that has been analytically well-constrained will still produce different μ^{142}Nd compositions for samples that should otherwise be genetically identical. This difference may be produced by small-scale geological processes, such as localized effects from high-temperature mass-independent isotopic fractionation [76], but are essentially untraceable. Higher-order geochemical heterogeneity that exists independent of this geological randomness can be statistically tested by grouping well-constrained samples using independent geochemical or geological data. Such an approach mirrors hierarchical "nested studies," which are commonly applied in biological and medical studies. For example, samples can be divided according to their isotopic grouping (FOZO, EM, and HIMU), according to island, or can be summarized on a per-hotspot basis. The success of each level of grouping can be assessed for example using Isoplot's probability of fit model. Evaluating all Marquesas samples together, the probability of fit for μ^{142}Nd is 0.08. Samples from the island Hiva Oa, which represent all isotopic groups, have a probability of fit of 0.2 for μ^{142}Nd. The highest probabilities of fit are returned when the samples are grouped according to their isotopic groups, which were determined by their He-Sr-^{143}Nd-Pb isotopic compositions (see discussion above). For the EM, HIMU, and FOZO groups, the probabilities of fit for μ^{142}Nd are 0.87, 0.56, and 0.54, respectively. The probability of fit for the combined EM and FOZO groups, which display more isotopic likeness than either of these groups compared to the EM group, is 0.76 for μ^{142}Nd. At all levels of grouping, the probabilities of fit for long-lived radiogenic isotopic systems (He-Sr-^{143}Nd-Pb) are very low, often <0.01. This is interpreted as an example of geological randomness as discussed above because these compositions are clearly analytically resolved and long-lived radiogenic isotopes display much more geological heterogeneity (parts per 10^4 or less) than short-lived radiogenic isotopes (parts per 10^5 or more). Changes in ε^{143}Nd could be locally induced in a single magma batch by, for example, chemical assimilation of materials with distinct ε^{143}Nd values during fractional crystallization, but such effects are virtually impossible to geologically constrain.

To verify that our techniques are able to resolve small-scale μ^{142}Nd heterogeneity like that observed between the EM and HIMU/FOZO groups of Marquesas OIB, an analytical "challenge" was designed (**Figure S9**). Using samples with previously well-constrained μ^{142}Nd compositions from each group, samples that displayed μ^{142}Nd signatures of opposite signs (positive vs. negative) were measured in sequence. In this challenge, samples HO-PUA-2 and HO-PUA-2 (EM), NH-HA-1 (FOZO), and HO-HI-3 (HIMU) were utilized. Given the internal precision of each run (1.8-2.8 ppm) and the 2σ standard deviation of all standards run in the

same session (1.3 ppm, n = 5), both EM samples are statistically resolved from the FOZO sample run before or after. The μ^{142}Nd composition of HIMU sample HO-HI-3 is likewise lower than that of each EM sample, but in this case the measurements were not statistically resolved. However, the μ^{142}Nd composition of HO-HI-3 determined during the challenge strongly overlaps with the 95% confidence interval of the combined HIMU and FOZO group. The μ^{142}Nd value of HO-HI-3 from this run represents one of the highest measured for this sample throughout the study. This result thus illustrates the importance of sample replication to achieve accurate results. These results neglect medium-term precision as the challenge was completed within a short timescale (6 days) whereas medium-term precision enables comparison of data collected over longer timescales (e.g., the lifespan of the Faraday cups). The overall result of the challenge within the context of medium-term precision can be projected using Isoplot's Model-2 function, which calculates a factor by which to expand the data precision to account for unknown, external controls on the true data precision. Using these calculations, the challenge produced a weighted average for EM sample runs of μ^{142}Nd = +3.4 ±1.1 (MSWD = 1.1) and for HIMU and FOZO samples of μ^{142}Nd = -1.5 ±2.4 (MSWD = 5.1; the high MSWD reflects the somewhat high μ^{142}Nd of sample HO-HI-3 measured during the challenge), thus confirming that the two groups are statistically distinct, even if samples from each group are run in sequence within short time proximity.

Chemical separation and isotopic measurements of Sr and Pb

Strontium and lead isotopic measurements were performed on the same sample powders, but represent different powder aliquots than those used for ^{142}Nd isotopic measurements due to differences in separation techniques. First, Pb was separated from sample matrix using BioRad® AG 1-X8, 100-200 mesh anion exchange resin using mixed solutions of HNO_3 and HBr. The residual Br^- in the sample matrix aliquot from this separation was then burned off using drops of concentrated HNO_3, and the sample was then re-equilibrated in HCl. Strontium and other minor elements (including Rb) were then separated from major elements using BioRad® AG 50W-X8, 200-400 mesh cation exchange resin using solutions of 2-2.5M HCl. The Sr-bearing aliquot from this separation was then re-equilibrated in HNO_3 and subjected to a final separation using Eichrom Sr resin and solutions of 0.05-4M HNO_3. Total procedural blanks for this method were ca. 370 pg for Sr and ca. 20 pg for Pb, which each represent <0.1% of sample Sr and Pb.

Isotopic compositions of Sr were measured on the Thermo Fisher Scientific Triton TIMS at the Isotope Geochemistry and Cosmochemistry group at ETH Zürich. Ratios of

$^{87}Sr/^{86}Sr$ were normalized to $^{88}Sr/^{86}Sr = 8.375209$ using the exponential law. The corrected sample $^{87}Sr/^{86}Sr$ ratios were then normalized to a $^{87}Sr/^{86}Sr$ ratio of 0.710245 (mean of published values from the GeoREM database) for the NBS987 standard on a per-session basis. The external precision of the measured $^{87}Sr/^{86}Sr$ ratios is estimated to be equivalent to the 2σ s.d. of all NBS987 standards run in the same session as the samples and is equal to 0.000010. The reference material BHVO-2 was measured twice in the same session as the samples and yielded a mean $^{87}Sr/^{86}Sr$ ratio of 0.703467 ±0.000007, which agrees with the preferred value of GeoREM (0.703478 ±0.000068). Strontium isotopic compositions for all standards, reference materials, and samples are summarized in **Table S5**.

Lead isotopic compositions were measured on the ThermoFisher Neptune inductively coupled plasma mass spectrometer (ICP-MS) of the Isotope Geochemistry and Cosmochemistry group at ETH Zürich. Instrumental mass fractionation was corrected using Tl doping and a $^{203}Tl/^{205}Tl$ ratio that is iteratively constrained in order to reduce the sum of offsets between the measured $^{206,207,208}Pb/^{204}Pb$ and $^{207,208}Pb/^{206}Pb$ compared to the standard NBS981 [77] to zero. The external precisions of measured $^{206}Pb/^{204}Pb$, $^{207}Pb/^{204}Pb$, and $^{208}Pb/^{204}Pb$ ratios, defined as the 2σ s.d. of all NBS981 standards run in a given session, were 0.0007-0.0019, 0.0007-0.0022, and 0.0020-0.0059, respectively, across three measurement sessions. Repeated measurements of the reference material BCR-2 yielded measured $^{206}Pb/^{204}Pb$, $^{207}Pb/^{204}Pb$, and $^{208}Pb/^{204}Pb$ ratios of 18.7665 ±0.0001 (GeoREM preferred: 18.754 ±0.018), 15.6323 ±0.0001 (GeoREM preferred: 15.622 ±0.010), and 38.7638 ±0.0004 (GeoREM preferred: 38.726 ±0.044), respectively, in 50 measurements across all three sessions. Repeated measurements of the reference material BHVO-2 yielded measured $^{206}Pb/^{204}Pb$, $^{207}Pb/^{204}Pb$, and $^{208}Pb/^{204}Pb$ ratios of 18.6195 ±0.0002 (GeoREM preferred: 18.634 ±0.068), 15.5417 ±0.0001 (GeoREM preferred: 15.524 ±0.050), and 38.2378 ±0.0004 (GeoREM preferred: 38.146 ±0.646), respectively, in 15 measurements across all three sessions. Lead isotopic compositions for all standards, reference materials, and samples are summarized in **Table S6**.

Enriched mantle (EM) mixing models

The EM dilution/mixing models presented in **Figure 3** are built on a simple mixing calculation between an assumed Marquesas FOZO-like component ($^{87}Sr/^{86}Sr = 0.7045$ and $\varepsilon^{143}Nd = +4.0$, cf., **Figures 1** and **S1**) and an extreme EM representative from the Samoa hotspot (sample ALIA115-21 from [34], cf. [42]). The EM component is selected as the recycled component for this mixing model because it has an elevated $\mu^{142}Nd$ composition compared to the presumed bulk Earth composition ($\mu^{142}Nd \equiv 0$), meaning that the bulk Earth composition

can be used as an endmember in the envisaged dilution process. By contrast, the Marquesas HIMU group has a μ^{142}Nd signature that strongly overlaps the bulk Earth value. This means that any mixing/dilution model involving HIMU would have to invoke two components with non-zero μ^{142}Nd signatures, but no independent basis exists for identifying what components these would be.

The mixing models for the Marquesas EM group invoke a Samoa-like EM composition as the presumed non-zero μ^{142}Nd endmember based on observed Sr-Nd-Pb isotopic correlations (**Figures S1-S2**). It is noted that the Fatu Hiva trends envisaged by [27] may not point directly toward a Samoa-like endmember (e.g., **Figure S2**). However, all EM-like samples in the Marquesas archipelago lie on the Ua Huka group trends. The Sr and Nd abundances of the FOZO endmember in this calculation were set to the primitive mantle values of [78]. The Sr and Nd concentrations of the EM endmember were set to the median abundances of felsic rock samples from the Baltic Shield, Dharwar Craton, Kaapvaal Craton, North Atlantic Craton, North China Craton, São Francisco Craton, Siberian Craton, Superior Province, and West Australian Craton, where both Rb and Sr or Sm and Nd abundance data were available. These medians were calculated using data available in the December 2023 versions of the precompiled data files of GEOROC, and no temporal trends for element abundance medians are observed across the Archean Eon (**Figure S10**). It is assumed that the Sr and Nd abundances of the subducting material are unchanged compared to the respective elemental abundances of the rocks they derived from; this is consistent with the nearly identical Sr and Nd abundances of modern upper continental crust [79] and subduction zone sediments [80], which implies that these elements behave conservatively during sedimentary processing (see also Figure 18 of [43]). The Pb isotopic compositions of EM lavas were not modeled because of the susceptibility of Pb and its isotopic compositions to modification by post-eruptive processes.

Once the Sr-^{143}Nd mixing curve was calculated, the closest point along this mixing line to the average of the Marquesas EM group samples was calculated to be ca. 0.6% of the EM endmember (i.e. ca. 99.4% dilution of this component by FOZO). The mixing line was then projected to μ^{142}Nd-ε^{143}Nd space using an assumed μ^{142}Nd of FOZO (μ^{142}Nd = -1, the average of the Marquesas FOZO group) and the highest μ^{142}Nd composition recorded by the Marquesas EM group samples (sample HO-PUA-2, μ^{142}Nd = +2.6), which was fixed to the same mixing proportion as for the Sr-^{143}Nd mixing model. The μ^{142}Nd mixing line was then projected to a 100% EM endmember, giving a resulting μ^{142}Nd value of +24. The uncertainty on this result (+10/-5) reflects the propagation of the 95% confidence intervals for the ^{87}Sr/^{86}Sr and ε^{143}Nd compositions of the Marquesas EM group. Model parameters are summarized in **Table S7**.

It is important to make two observations about this mixing model. First, it presumes that the EM endmember is comprised only of felsic material (after [42]), whereas the rocks with the highest published μ^{142}Nd values ($\geq$ +16.9, n = 8, [44-46, 81]) are exclusively mafic. Second, the formation of Archean felsic crust presumes the existence of a mafic precursor [4], and thus that Earth's earliest crust must have been mafic before it became felsic. The zircon record implies that felsic material was present at Earth's surface by 4.4 Ga [6], but it is reasonable to assume that a large fraction of mafic material remained at Earth's surface at the end of the Hadean Eon (4 Ga ago). We therefore calculate a refined model to predict compositions of mafic and felsic members of materials subducted into the Marquesas deep mantle source (**Figures S3-S4**). For simplicity, it is assumed that the felsic member is a direct product of melting of the mafic endmember, since the two materials would be expected to be spatially proximate [36]. In order to calculate the reciprocal Nd isotopic compositions of these endmembers, a differentiation chronology must be defined (**Figure S4**). It is assumed that initial mantle differentiation to produce an early depleted mantle reservoir occurred 4.37 Ga ago, a globally isochronous date in the Sm-Nd system among Archean-aged rocks [59]. It is further assumed that the final felsic member was formed at 4.1 Ga and that it evolved a μ^{142}Nd composition of +16, equal to the highest value measured for a felsic rock [44], and a modern ε^{143}Nd composition of -32, which overlaps the value for Archean crustal composites [82]. The mafic sedimentary member is presumed to have a chondritic modern ε^{143}Nd composition and Sr and Nd abundances equal to the median of compiled cratonic rocks (using the same GEOROC precompiled files are previously mentioned; **Figure S11**). Like felsic rocks, there are no temporal trends in the Sr and Nd abundances of Archean-Proterozoic mafic rocks (**Figure S11**), so the use of these abundances is considered broadly representative. The timing at which the mafic sedimentary member was extracted from the early depleted mantle reservoir was used as a fitting parameter, as described below. Given these constraints, the mafic sedimentary member must have had a μ^{142}Nd value of $+27^{+12}_{-7}$ and subducted material must be ca. 93% mafic. The proportion of mafic sediment would be less if the felsic sediment member had a higher positive μ^{142}Nd value or a lower Nd abundance. Dilution of this endmember with primitive component represented by the Marquesas FOZO sample group produces a mixing array that intersects the Marquesas EM group Sm-Nd compositions (**Figure S3**). Because the Sr and Nd abundances of the mafic and felsic sedimentary members affect the elemental composition of the bulk modeled sediment, the total mixing proportion of sediment increases to 1-2% (cf., [28, 30])

The chronology and resulting Nd isotopic compositions of the refined model are calculated using a series of error minimization calculations. First, the required fraction of the

mafic member required to match the ε^{143}Nd composition of the EM endmember composition from the first model is calculated given the inputs mentioned above. This fraction is then used to recalculate the Sr-^{143}Nd mixing relationship as in the first mixing model and determine the required μ^{142}Nd composition of the mafic sedimentary member. Second, the Sm/Nd ratio of the early depleted mantle reservoir is calculated using the assumed time of mantle differentiation (4.37 Ga ago) and to fit the calculated μ^{142}Nd composition of the mafic sedimentary member that is eventually extracted from this early depleted mantle reservoir. Then, the Sm/Nd ratio of the extracted mafic magma is calculated to satisfy the assumption that it evolves to a modern chondritic ε^{143}Nd composition. These calculations are then iterated to produce a mafic magma matching both the required μ^{142}Nd and ε^{143}Nd compositions. Third, the Sm/Nd ratio of the felsic sedimentary member is calculated assuming that it evolves to a modern ε^{143}Nd composition of -32. Then, the time at which the mafic material is re-melted to form felsic rock is adjusted to match the highest μ^{142}Nd in the current rock record (ca. +16, [44]). These two calculations are then iterated to produce a felsic rock matching both the required μ^{142}Nd and ε^{143}Nd compositions. The uncertainty on the μ^{142}Nd compositions produced by this model were calculated analogously to the first mixing model. All model inputs and intermediate outputs are summarized in **Table S7**.

The μ^{142}Nd compositions required for the sedimentary components of both the first and refined models are similar to or somewhat higher than the highest measured μ^{142}Nd values for any global Archean-aged rock (**Figure S5**). In all global Archean cratons, the highest μ^{142}Nd signatures are observed early, mostly in the Eoarchean Eon (**Figure S5a**). By extension, the μ^{142}Nd values required by the models were only present on Earth in the Eoarchean and before, with the highest probability of materials possessing μ^{142}Nd $\geq$+20 before the Archean-Hadean boundary (4 Ga ago). Very few rocks older than 4 Ga old have been measured for μ^{142}Nd, likely because they have all been remelted or destroyed by erosion or tectonic processes. As time progresses, it is increasingly unlikely that any segment of Archean crust that is eroded in a spatially stochastic manner will result in a sediment with a high, positive μ^{142}Nd signature. This is illustrated by the cumulative average μ^{142}Nd compositions of published data, which show that even the average Eoarchan rock had a μ^{142}Nd composition of only ca. +10. It is thus very unlikely that subduction of sedimentary material with the bulk μ^{142}Nd composition required by the models (+24 in the first model and +27 for mafic material in the refined model) would have occurred in the Eoarchean or later.

Both models assume that the Marquesas EM endmember is represented by an extreme Samoa-like Sr-^{143}Nd-Pb isotopic composition. This would seem to imply that the results of the

models predict that Samoa EM-type lavas should have strongly elevated μ^{142}Nd signatures. However, this assumption is invalid for several reasons. First, although the EM arrays of many global hotspots overlap (e.g., the Pitcairn trend and Koʻolau group of Hawaiʻi), their heritages are often considered to be independent of one another [29, 83], for example representing sedimentary packages of unique blends (e.g., pelagic versus continental) and ages. Second, the mildly elevated $^{3}He/^{4}He$ signature of Marquesas EM group lavas [40] contrasts with the sub-MORB $^{3}He/^{4}He$ ratios of Samoa [34]. The two distinct signatures can be reconciled if the EM components of each hotspot have contrasting He abundances (as illustrated in **Figure S2**), however this would imply that they have distinct heritages. Finally, Archean-aged felsic crust is characterized by variable, but uniformly high $^{87}Sr/^{86}Sr$ ratios, low $^{143}Nd/^{144}Nd$ ratios (e.g., [82]), and radiogenic Pb isotopic compositions (e.g., [84], for bulk crust). Despite this, Archean-aged crust has highly heterogeneous μ^{142}Nd compositions (e.g., [36, 44]). This occurs because long-lived radiogenic isotope systems, such as ^{87}Rb-^{87}Sr and ^{147}Sm-^{143}Nd, are decoupled from short-lived systems, such as ^{146}Sm-^{142}Nd, during any melting or differentiation event that occurred after the lifetime of ^{146}Sm (ca. 500 Ma, i.e. after ca. 4 Ga ago). Events such as melting and metamorphism are fundamental parts of crustal building and will strongly affect Sr-^{143}Nd isotopic compositions while it is often assumed that they leave μ^{142}Nd compositions unchanged. Such isotopic decoupling is therefore a natural consequence of crustal building throughout the Archean. For these reasons, it is possible that the Marquesas and Samoa EM endmembers have Sr-^{143}Nd-Pb isotopic compositions that are broadly similar, but with distinct μ^{142}Nd compositions. One submarine lava sample from Samoa with an EM-like isotopic signature has been measured to date, and it did not display an anomalous μ^{142}Nd composition [16]. The Marquesas EM component may therefore be unique in this respect and may only be sampled because of the low melt production of the Marquesas hotspot, or other EM hotspots may possess heterogeneous μ^{142}Nd signatures, but these have not yet been discovered because high-precision techniques have not yet been applied to these hotspots.

Simulation of the μ^{142}Nd compositions of subducted sediments

Figure 4d presents a simulation for the expected μ^{142}Nd compositions of subducting sediments at different times through Earth's history. The model is constructed utilizing a compilation of global μ^{142}Nd data (see following section for information and references) of all lithological types. Although the Sr-^{143}Nd-Pb isotopic compositions of Marquesas OIB are consistent with contributions from felsic sediments in particular, there is no systematic difference between the μ^{142}Nd compositions of felsic and other lithologies (**Figure 4c**). Data

for all lithologies were therefore included to increase the representativeness of the dataset. First, in order to account for the extreme rarity of μ^{142}Nd compositions ≥ +19 (ca. 0.6% of all published data), the dataset was corrected for potential preservation bias. As discussed in the main text, preservation bias cannot be expected to account for the presence or absence of particular μ^{142}Nd compositions; instead, it can be expected that preservation bias stochastically affected materials of all μ^{142}Nd compositions. The effect of stochastic erosion would be to lessen the available mass of rocks of all μ^{142}Nd; since highly anomalous μ^{142}Nd values are relatively rare, stochastic erosion may therefore eliminate the most extreme μ^{142}Nd values from the rock record, thus narrowing the total extent of preserved μ^{142}Nd compositions. To counter this effect, the μ^{142}Nd values in our compiled dataset were dilated by a factor of 2.

Next, the complete dataset was sliced according to measured or inferred age of each sample to obtain sub-datasets representing all μ^{142}Nd data equal to or older than the age of a given timestep (0.1 Ga increments from 4.0 Ga to present). This simulates the integrated array of μ^{142}Nd compositions that would have accumulated at Earth's surface at the age of any given timestep. However, given the paucity of data for samples older than 3.9 Ga (<3% of all data), the age window was extended to include ages up to 0.3 Ga younger than a given timestep. For example, for the timestep at 3.5 Ga, data with ages ≥3.2 Ga were included. This age window was applied to all timesteps for consistency even though the effect of data paucity is most acute for the timesteps at 3.9 and 4.0 Ga. If this measure is not applied, the calculated probabilities of subducting sediments with average μ^{142}Nd ≥ +19 at 4.0 Ga are close to zero, since the only available dataset of this age reflects negative μ^{142}Nd compositions [85]. Following this, the probability of subducting sediments with μ^{142}Nd ≥ +19 at the 3.8 Ga timestep is markedly higher, thus contradicting the trend toward lower μ^{142}Nd values over time that is clearly present in the global dataset (**Figure 4a**). Note that even when the age window is extended as described above, the calculation at the 4.0 Ga timestep is clearly affected by data paucity within its age window.

The age-windowed sub-datasets were then bootstrapped to obtain expanded datasets of 10,000 members. To simulate stochastic erosion and recycling of sediments, 20,000 simulations were then performed in which 10 members of the bootstrapped sub-datasets were selected at random with replacement (a simplified Monte Carlo method). The μ^{142}Nd compositions of these 10 members were then averaged to obtain the predicted μ^{142}Nd composition of the total recycled sedimentary package. The probability of obtaining a recycled sedimentary package with μ^{142}Nd ≥ +19 is calculated by dividing the number of cases where the average of the 10 selected members was ≥ +19 with the total number of simulations (20,000). Since the absolute value of

this probability is compromised by the dilation correction described previously, the probabilities are internally normalized, such that the highest probability is assigned a value of 1. The absolute probabilities are displayed in **Figure 4d** as guidance only, to illustrate that the probability of recycling sediments with average $\mu^{142}Nd \geq +19$ at 4.0 Ga is still relatively low based on presently published $\mu^{142}Nd$ data.

References for ^{142}Nd compilation in Figure 4

The global compilation of $\mu^{142}Nd$ in Figure 4 is not intended to be exhaustive, but it represents all studied environments and comprises the vast majority of all published data. Data sources: [16, 19, 36, 44-47, 49, 58, 59, 81, 85-104].

Figures

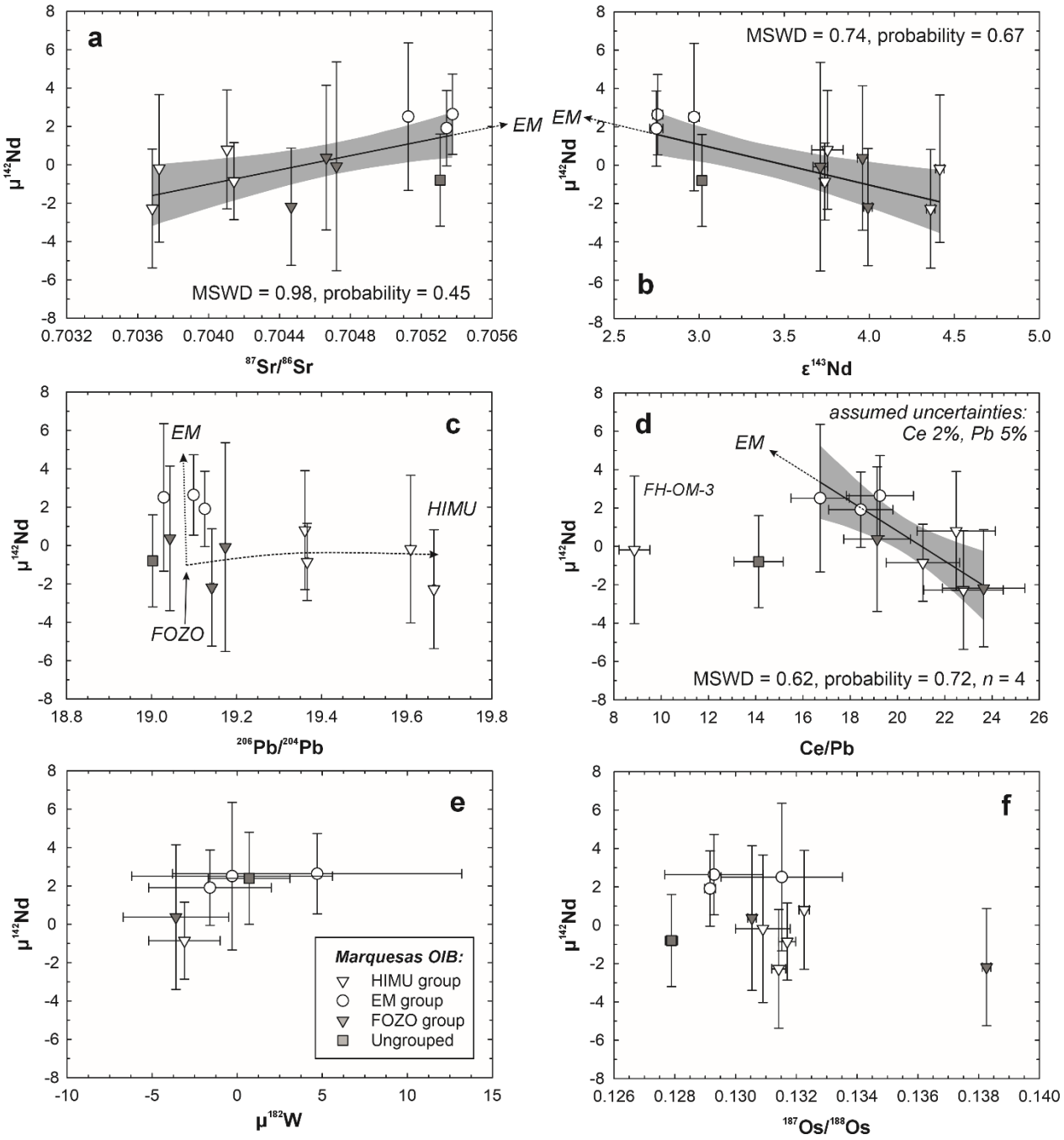

Figure S1. Relationships between the $\mu^{142}Nd$ and other geochemical and isotopic proxies for the involvement of distinct mantle components in the source of Marquesas lavas. Where correlations are statistically significant, these are illustrated by bold lines and shaded regions showing the 95% confidence level of the correlation, both calculated using Isoplot [33]. Note that, despite nearly all samples have statistically indistinguishable $\mu^{142}Nd$ compositions, the strong variability of the abscissa variables (except for $\mu^{182}W$, panel e) means that the two-dimensional correlations are built on statistically independent points (i.e. their error ellipses do not statistically overlap). This is further evidenced by robust MSWD and probabilities of fit. For $\mu^{142}Nd$ vs. $^{206}Pb/^{204}Pb$ ratios (panel

c), a correlation is precluded by the very similar Pb isotopic compositions of FOZO- and EM-group samples, which nevertheless have distinct μ^{142}Nd signatures. The qualitative senses of data trends are outlined by dashed lines. For μ^{142}Nd versus Ce/Pb ratios (panel d), the uncertainty on Ce/Pb ratios is calculated assuming 2% uncertainty for Ce and 5% uncertainty for Pb, which are typical for bulk trace element analyses. This produces the minimum number of statistically distinct correlation points between panels a, b, and d, with $n = 4$ in the case of panel d. Additionally, sample FH-OM-3 is excluded from this correlation and we note that the Ce abundances for this sample published in [40] and [28] disagree with each other by a factor of ~5 (Pb abundances were not reported in [40]).

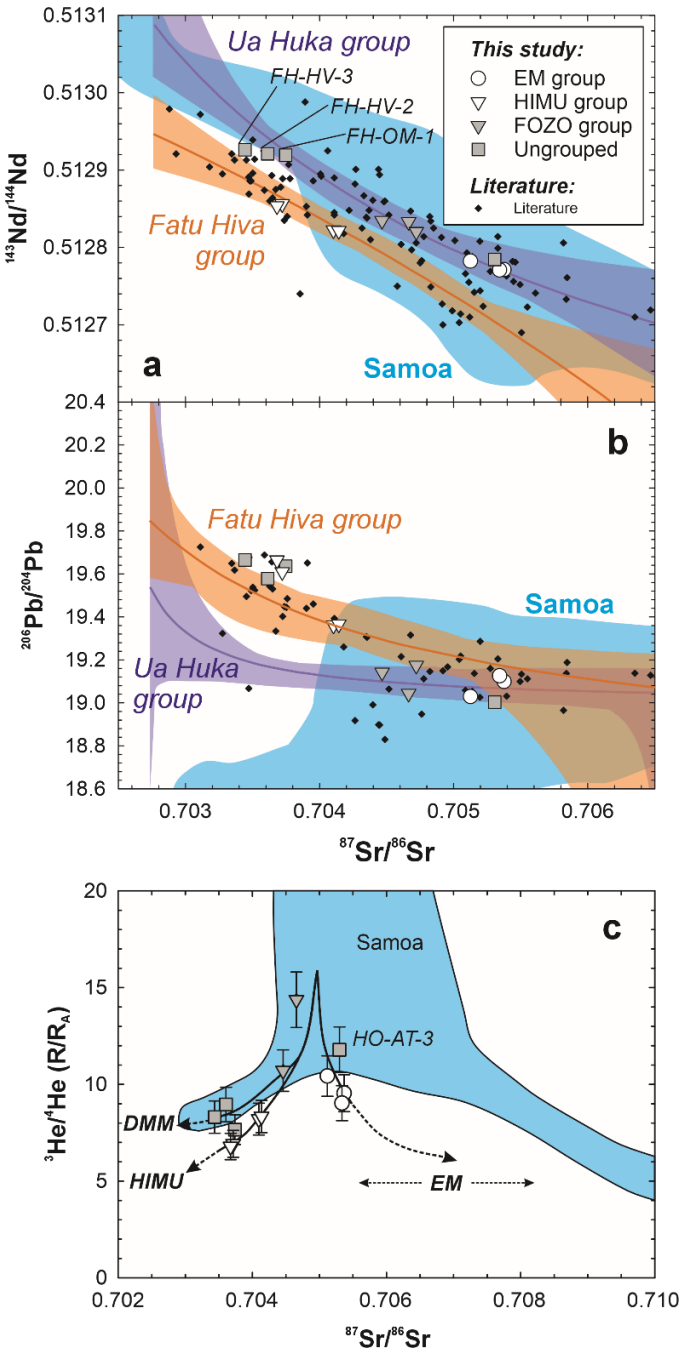

Figure S2. Long-lived radiogenic isotopic compositions of Marquesas samples in this study compared to literature data for Marquesas lavas [27, 62-64]. Best fit regressions for the Ua Huka and Fatu Hiva groups of [27] along with outlined regions encompassing all regression curves from [27] are shown for reference. Distinct trends for HIMU- and EM-group samples in panel c reflect the fact that EM and HIMU are not known to directly mix, but rather are only associated through a FOZO component (e.g., [37]). Illustrative mixing trends between a FOZO-like component and HIMU or EM through data for Marquesas OIB are shown. The trend of Marquesas EM-type lavas outside the field of Samoa implies that the two EM endmembers of these two hotspots must have distinct Sr and/or He abundances, but not necessarily that their EM endmember has a distinct He-Sr isotopic composition. Reference data for Samoa basalts is from the GEOROC database precompiled file (December 2023 version).

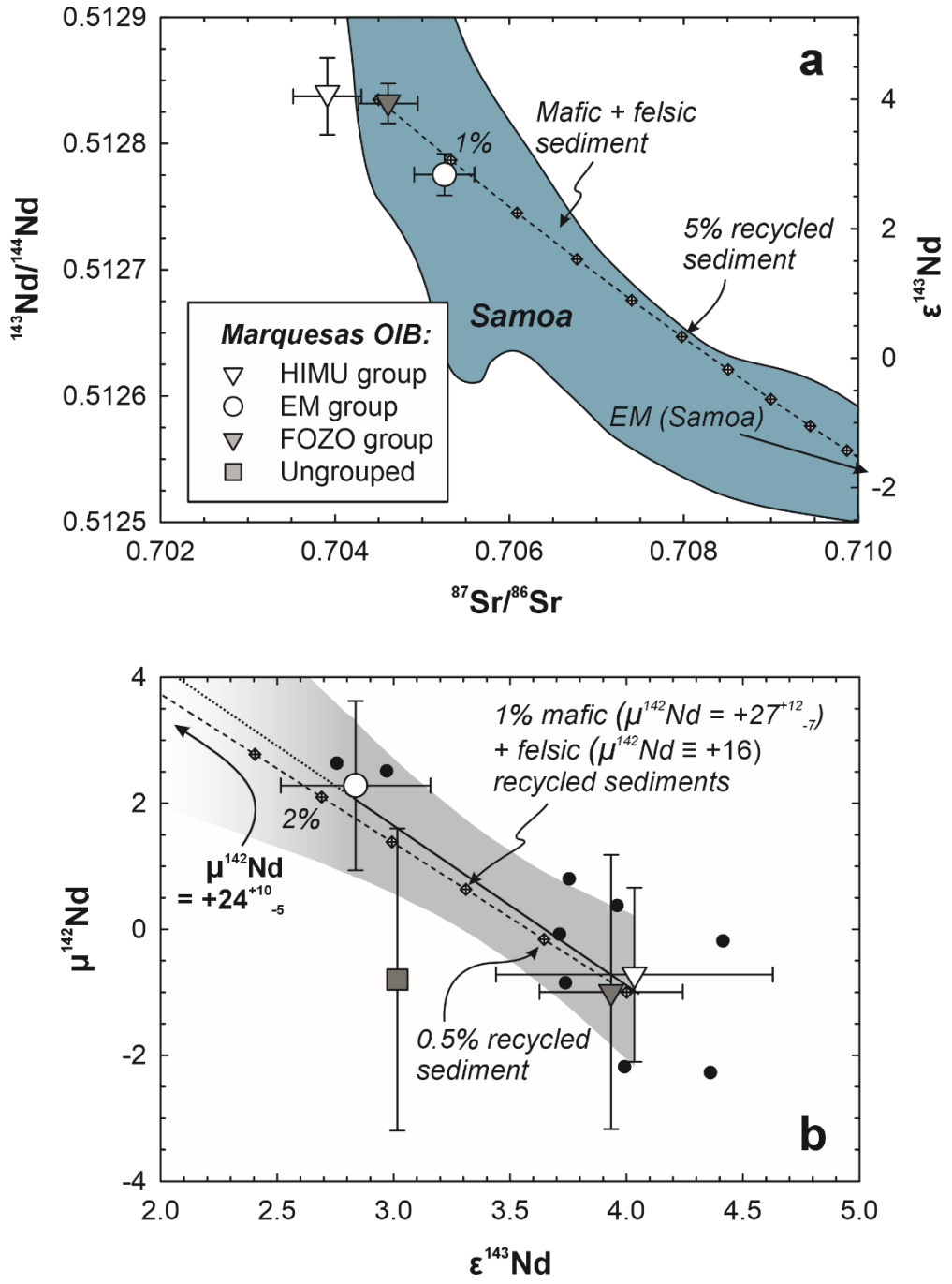

Figure S3. Refined model for the Sr-Nd isotopic compositions of Marquesas lavas calculating the compositions of mafic and felsic sedimentary members to the EM endmember (cf., **Figure 3**). The solid black line and gray shaded region represents the York-type linear regression and 95% confidence interval, respectively, of the μ^{142}Nd-ε^{143}Nd compositions of all samples [33]. The dotted black line and tapered gray shading represent an extrapolation of this regression. Large symbols and error bars show the per-group average and 95% confidence intervals, black circles show the per-sample measurements. The fraction of mixed EM component is noted by diamonds along the dashed mixing line. The compositional range of Samoa EM-type lavas is shown by the blue field in panel a with a reference to the assumed endmember Samoa Sr-^{143}Nd isotopic composition from sample ALIA D115-21 [34].

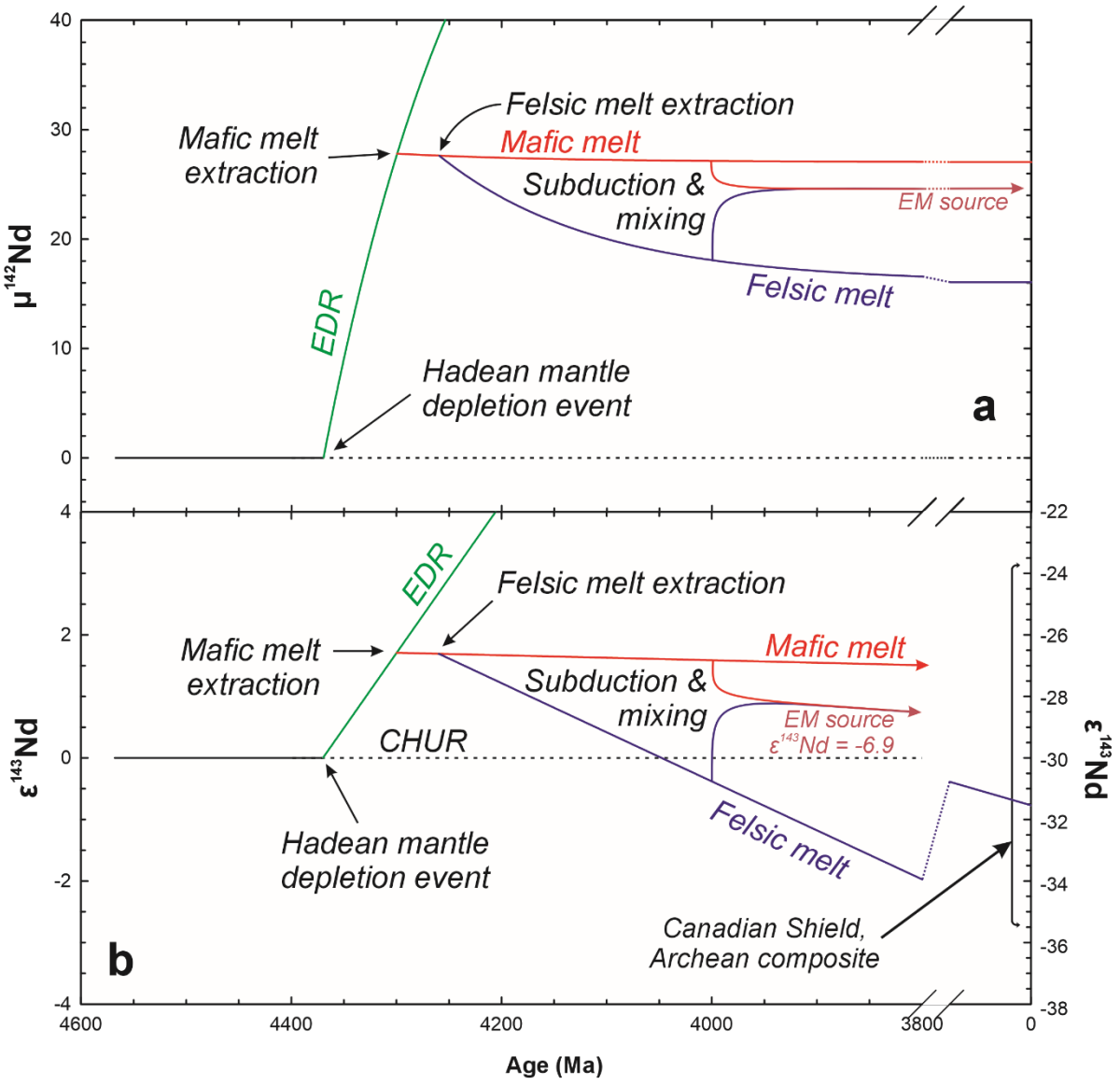

Figure S4. Assumed chonological evolution of the mafic and felsic components of the model shown in **Figure 3** and described in the main and supplementary texts. The model begins with a bulk Earth-like composition ($\mu^{142}Nd \equiv 0$) that is then differentiated during an event ca. 4.37 Ga ago, which is recorded in the Sm-Nd isotopic compositions of many global cratons [59], forming a depleted mantle domain. A mafic melt is then extracted from this depleted domain 4.26 Ga ago, and a felsic melt is produced from this mafic material at 4.1 Ga. For simplicity, it is assumed that the mafic and felsic materials reflecting the same chronological history are subducted together to form the Marquesas EM endmember, and possess a modern $\varepsilon^{143}Nd$ composition identical to that of extreme Samoa sample ALIA D115-21 [42]. The range of Archean crust composites in panel b is from [82].

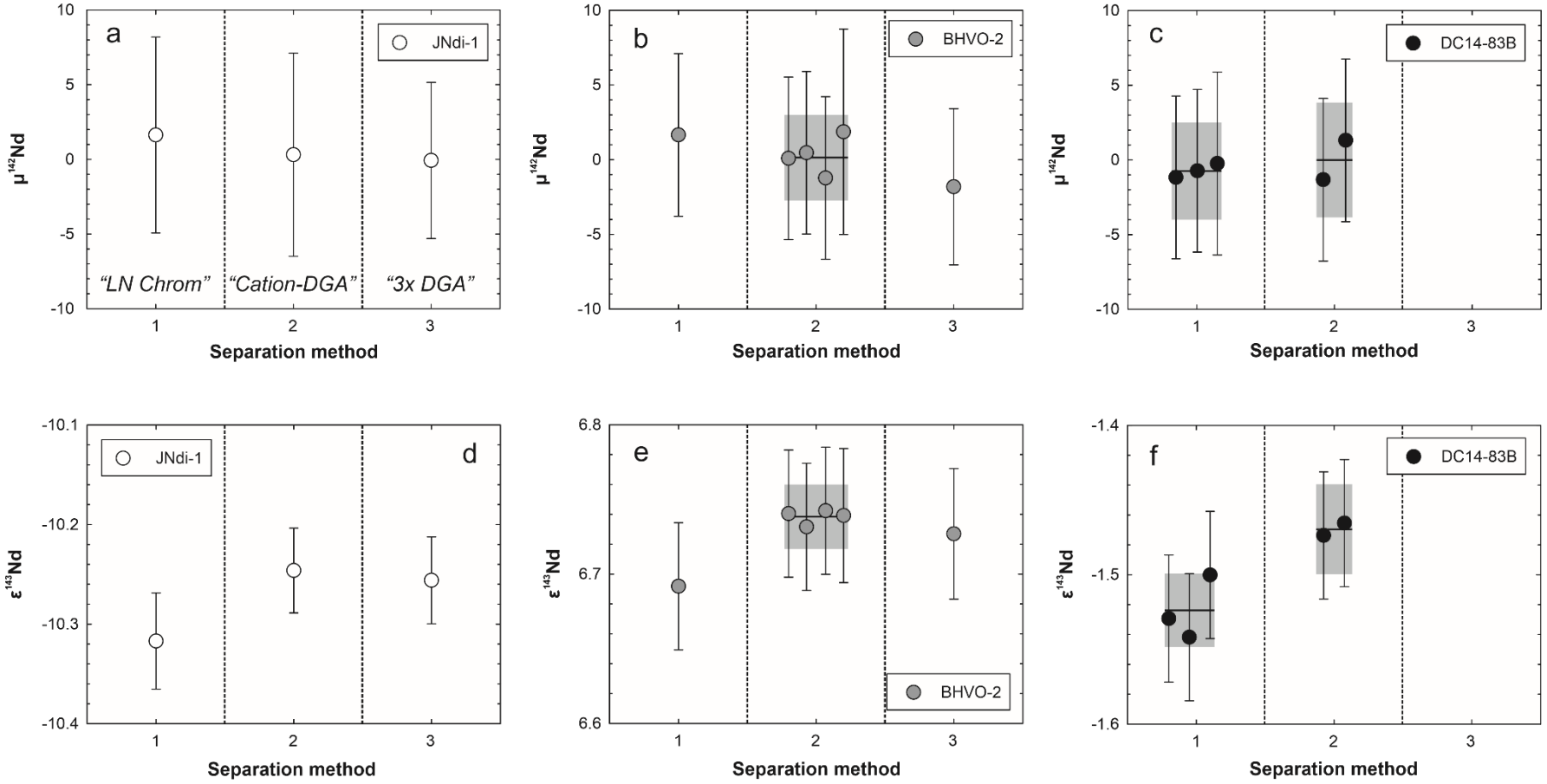

Figure S5. Comparison of Nd isotopic ratios measured in standard JNdi-1, United States Geological Survey reference material BHVO-2, and in-house reference material DC14-83B (lamprophyre, Deccan Traps) after processing through the three chemical separation methods described in the text.

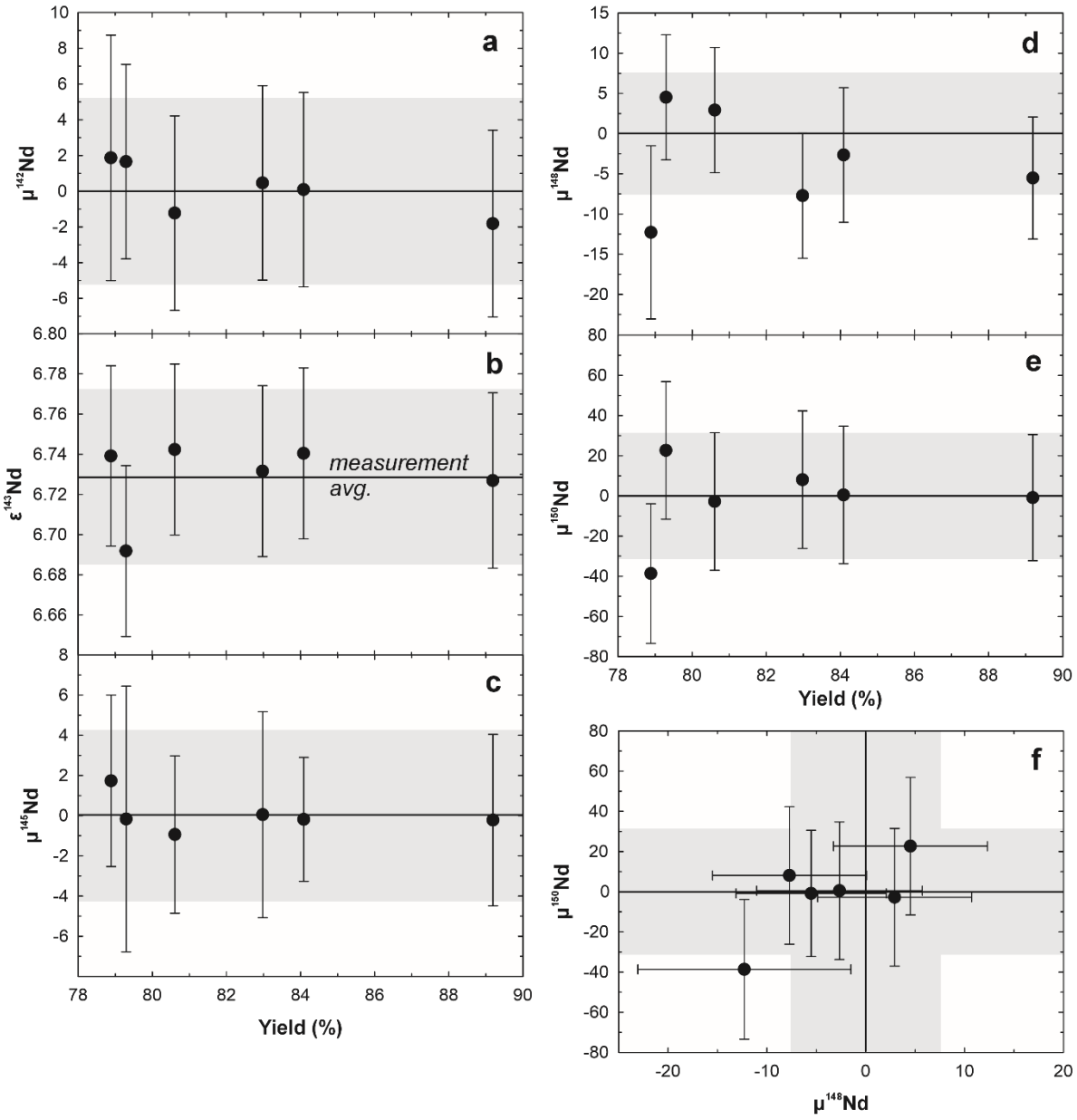

Figure S6. Comparison of yields for replicate aliquots of BHVO-2 versus Nd yield from separation chemistry. In all cases, no systematic trend is observed, except potentially for one sample processed using a long-aspect LN resin column (see text for details).

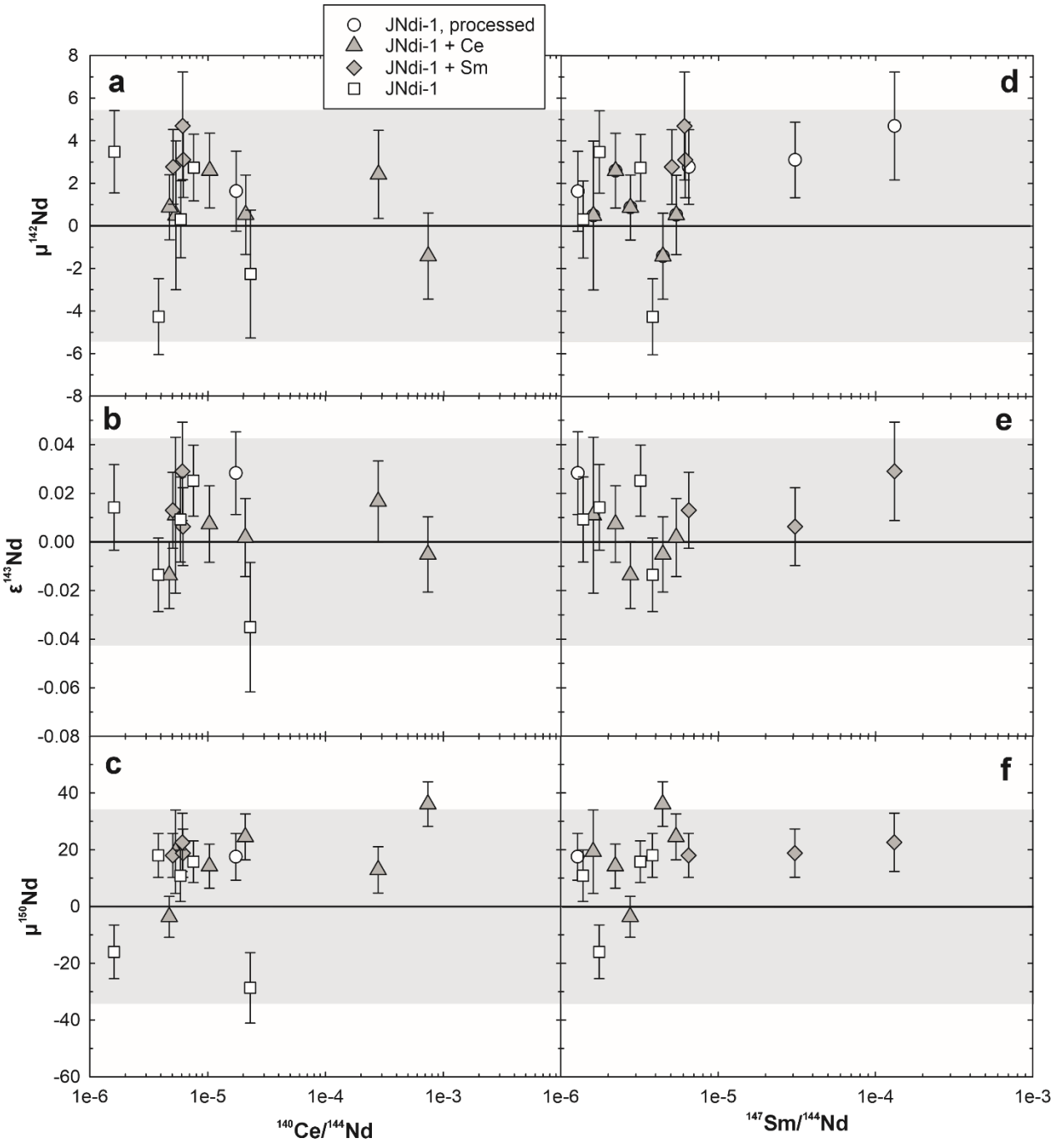

Figure S7. Neodymium isotopic compositions of JNdi-1 standards with and without added Ce or Sm dopants. In all cases, no trends are observed outside of analytical uncertainty, and in all cases measured sample $^{140}Ce/^{144}Nd$ and $^{147}Sm/^{144}Nd$ ratios were less than the maximum doped ratio displayed in this figure. In this figure, error bars represent the 2σ standard error of each measurement and the gray shaded region represents the medium-term analytical precision for each isotope ratio.

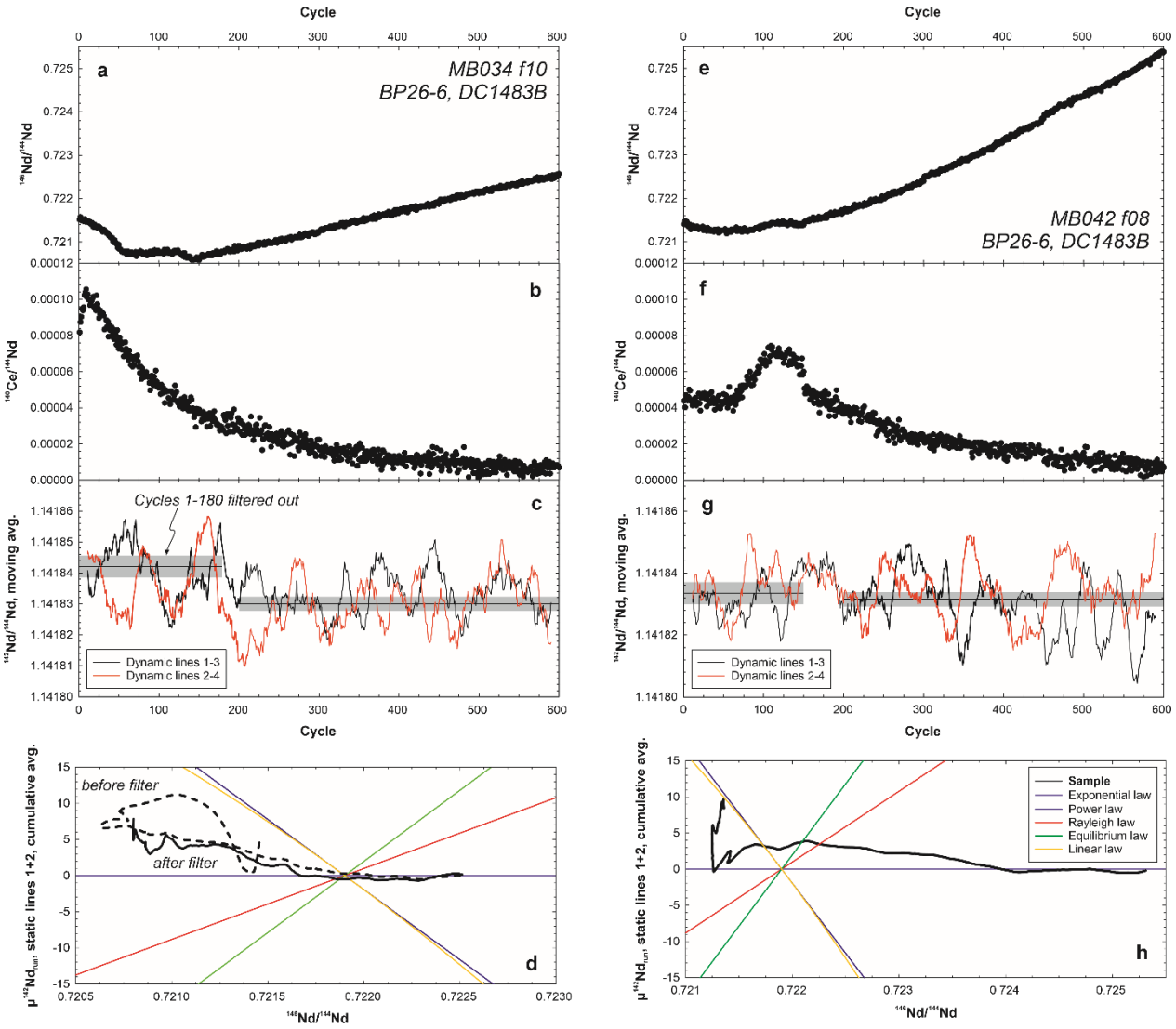

Figure S8. Example of data filtering for two replicate measurements of the same digestion of in-house reference material DC14-83B. The evolution of uncorrected $^{146}Nd/^{144}Nd$ ratios through the run is non-linear for the first ca. 25% of each run, implying that the corrected isotopic data could preserve mass-dependent isotopic effects, for example from domain mixing (e.g., [72]). In the first case (panels a-d), this is evident from higher $^{142}Nd/^{144}Nd$ ratios measured in cycles 1-180 and from possible non-exponential fractionation effects recorded in static $^{142}Nd/^{144}Nd$ ratios (panel d). These measurement cycles were thus removed from the data correction. However, in the second case (panels e-h) no effect on $^{142}Nd/^{144}Nd$ ratios (or any other Nd isotopic ratio) is observed, nor do static $^{142}Nd/^{144}Nd$ ratios evolve in a pattern parallel to non-exponential fractionation (panel h), and thus no data filtering is undertaken for this run.

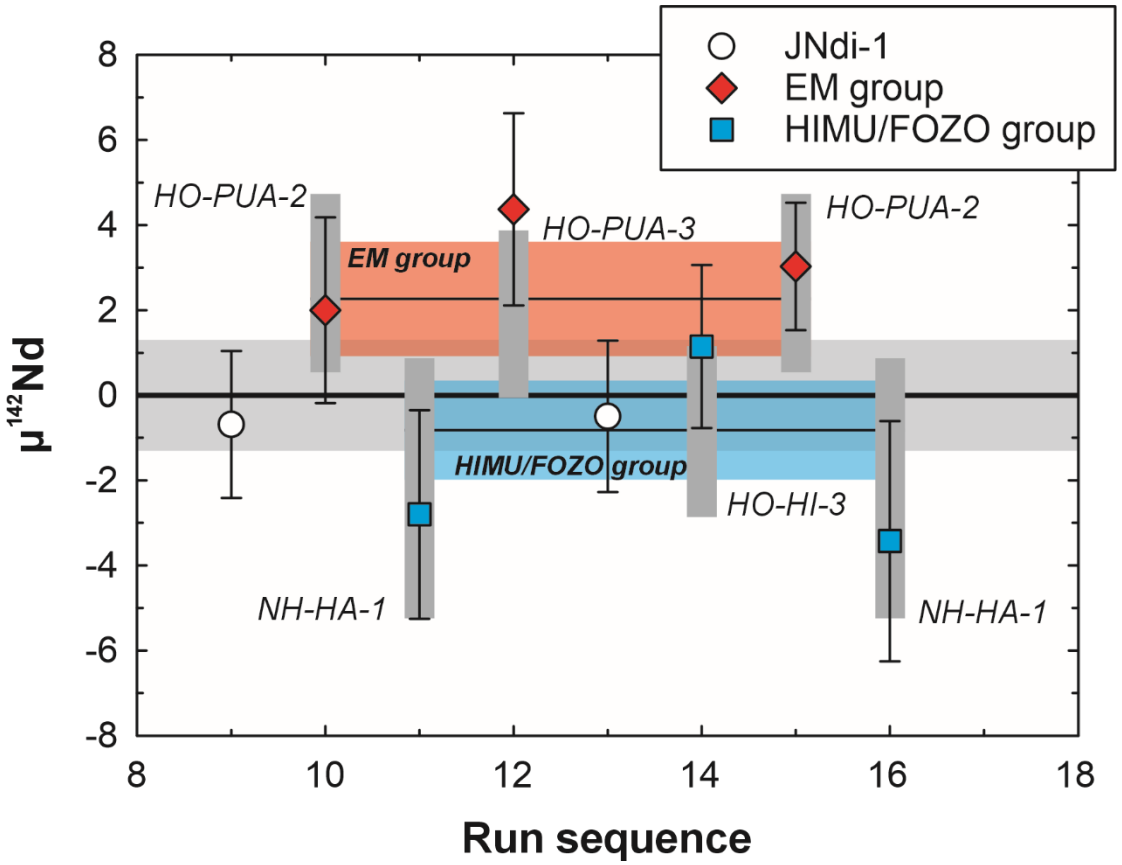

Figure S9. Results of the sample 'challenge' described in the Supplementary Information. Samples are plotted in run order to emphasize the ability of the mass spectrometer to resolve the $\mu^{142}Nd$ compositions of compositionally distinct samples in a short time period. Error bars represent 2σ s.e.m., vertical dark gray shaded boxes represent the 95% confidence intervals of all runs for each sample, and the horizontal light gray shaded region represents the 2σ s.d. of all standards run in the same session.

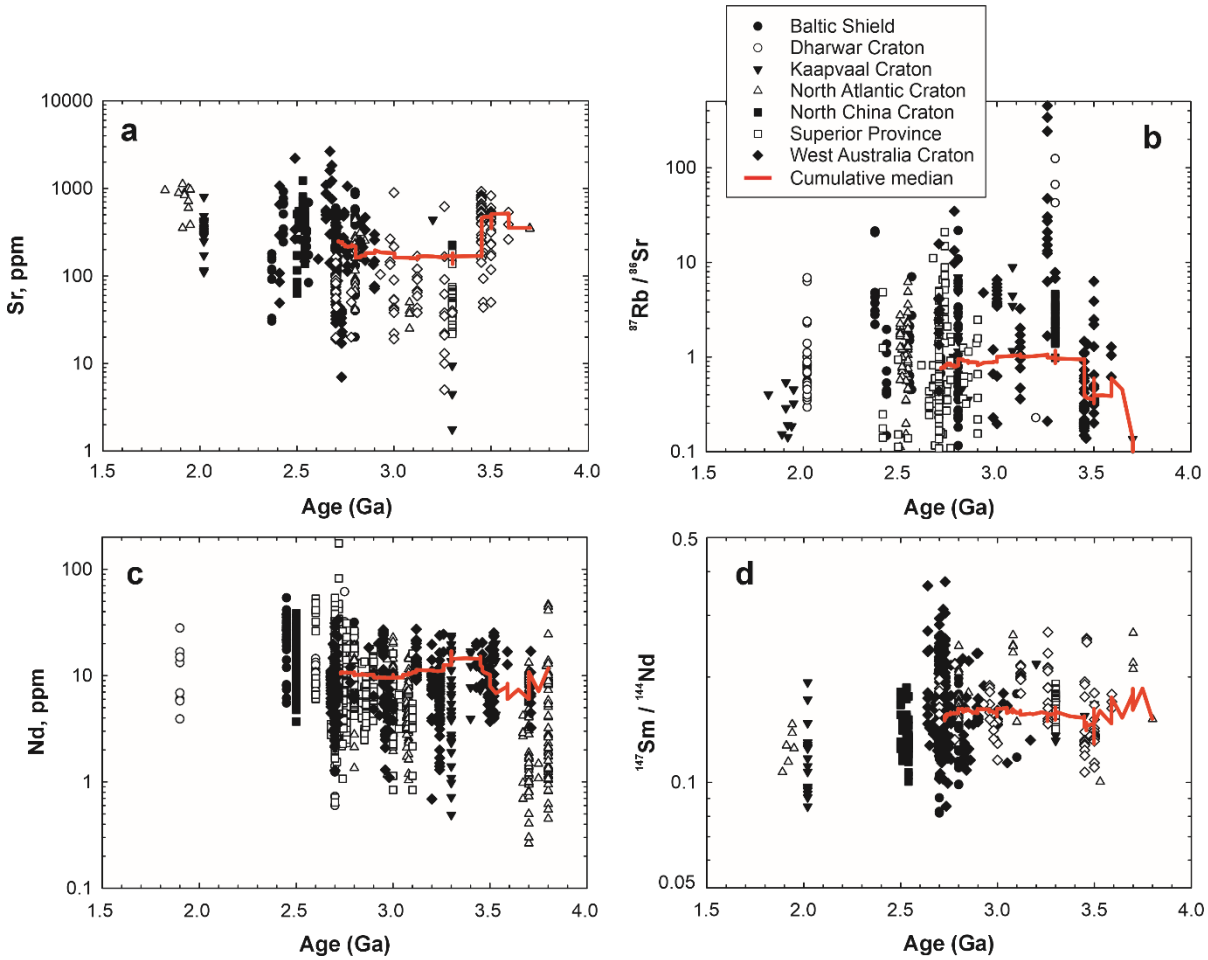

Figure S10. Abundances of Sr and Nd, Rb/Sr and Sm/Nd ratios for compiled felsic rocks from global cratons. Cumulative medians are shown by thick red lines, demonstrating no significant temporal change in the data across the Archean Era (4.0 to 2.5 Ga ago). Data assembled from the precompiled files of GEOROC (version December 2023).

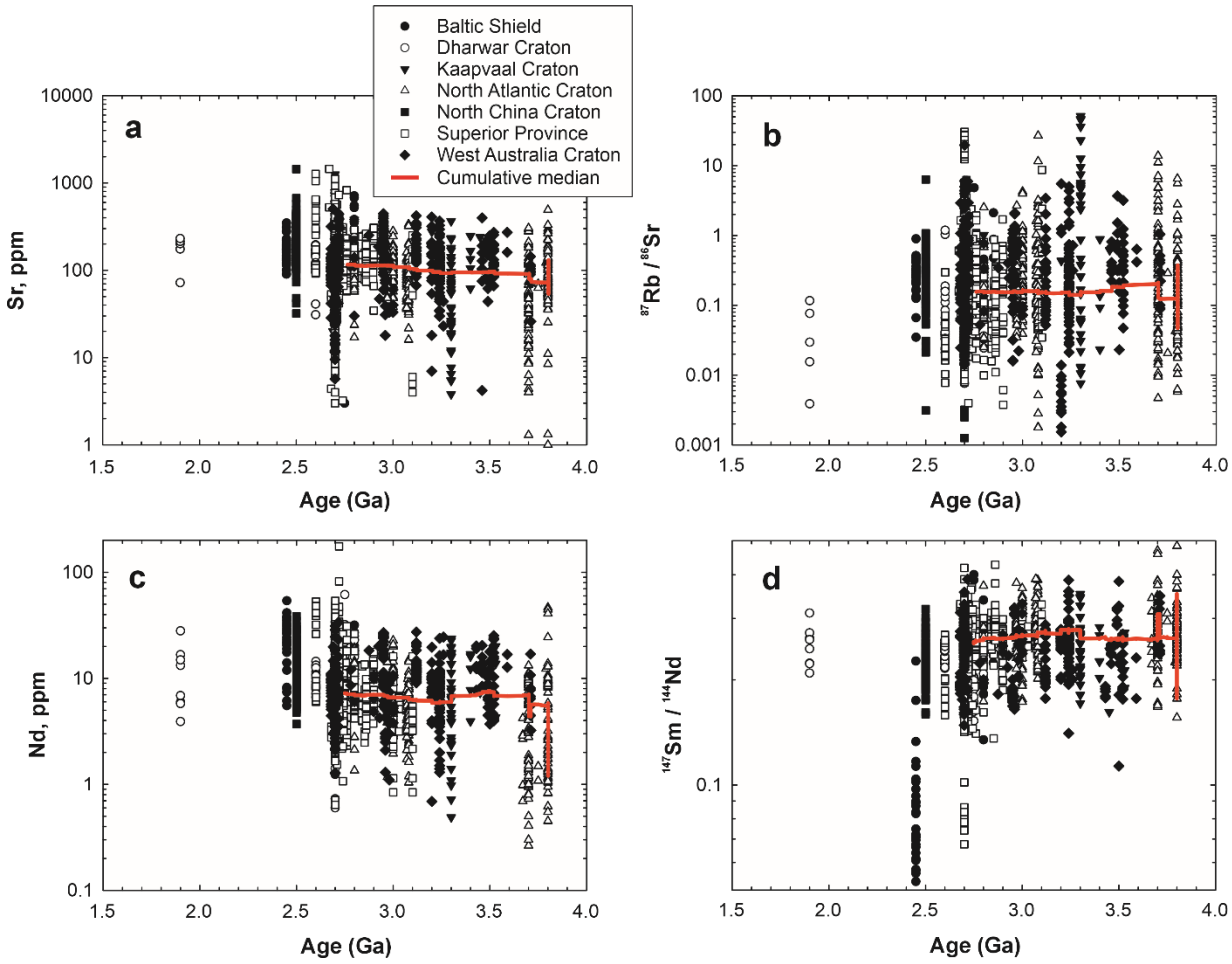

Figure S11. Abundances of Sr and Nd, Rb/Sr and Sm/Nd ratios for compiled mafic rocks from global cratons. Cumulative medians are shown by thick red lines, demonstrating no significant temporal change in the data across the Archean Era (4.0 to 2.5 Ga ago). Data assembled from the precompiled files of GEOROC (version December 2023).

References

1. Foley, B.J., *The Role of Plate Tectonic–Climate Coupling and Exposed Land Area in the Development of Habitable Climates on Rocky Planets.* The Astrophysical Journal, 2015. **812**(1).
2. Stern, R.J. and T. Gerya, *Subduction initiation in nature and models: A review.* Tectonophysics, 2018. **746**: p. 173-198.
3. Brown, M., T. Johnson, and N.J. Gardiner, *Plate Tectonics and the Archean Earth.* Annual Review of Earth and Planetary Sciences, 2020. **48**(1): p. 291-320.
4. Martin, H., *Petrogenesis of Archean trondhjemites, tonalites, and granodiorites from eastern Finland: major and trace element geochemistry.* Journal of Petrology, 1987. **28**(5): p. 921-953.
5. Wilde, S.A., J.W. Valley, W.H. Peck, and C.M. Graham, *Evidence from detrital zircons for the existence of continental crust and oceans on the Earth 4.4 Gyr ago.* Nature, 2001. **409**: p. 175-178.
6. Turner, S., S. Wilde, G. Worner, B. Schaefer, and Y.J. Lai, *An andesitic source for Jack Hills zircon supports onset of plate tectonics in the Hadean.* Nat Commun, 2020. **11**(1): p. 1241.
7. Guo, M. and J. Korenaga, *The combined Hf and Nd isotope evolution of the depleted mantle requires Hadean continental formation.* Science Advances, 2023. **9**.
8. McCoy-West, A.J., P. Chowdhury, K.W. Burton, P. Sossi, G.M. Nowell, J.G. Fitton, A.C. Kerr, P.A. Cawood, and H.M. Williams, *Extensive crustal extraction in Earth's early history inferred from molybdenum isotopes.* Nature Geoscience, 2019. **12**(11): p. 946-951.
9. Johnson, T.E., M. Brown, N.J. Gardiner, C.L. Kirkland, and R.H. Smithies, *Earth's first stable continents did not form by subduction.* Nature, 2017. **543**(7644): p. 239-242.
10. Smithies, R.H., Y. Lu, T.E. Johnson, C.L. Kirkland, K.F. Cassidy, D.C. Champion, D.R. Mole, I. Zibra, K. Gessner, J. Sapkota, M.C. De Paoli, and M. Poujol, *No evidence for high-pressure melting of Earth's crust in the Archean.* Nat Commun, 2019. **10**(1): p. 5559.
11. Wang, Q. and S.A. Wilde, *New constraints on the Hadean to Proterozoic history of the Jack Hills belt, Western Australia.* Gondwana Research, 2018. **55**: p. 74-91.
12. Stern, R.J., *The Orosirian (1800–2050 Ma) plate tectonic episode: Key for reconstructing the Proterozoic tectonic record.* Geoscience Frontiers, 2023. **14**(3).
13. Brown, M., T. Johnson, and C.J. Spencer, *Secular changes in metamorphism and metamorphic cooling rates track the evolving plate-tectonic regime on Earth.* Journal of the Geological Society, 2022. **179**.
14. Windley, B.F., T. Kusky, and A. Polat, *Onset of plate tectonics by the Eoarchean.* Precambrian Research, 2021. **352**.
15. Copley, A. and O.M. Weller, *Modern-style continental tectonics since the early Archean.* Precambrian Research, 2024. **403**.
16. Horan, M.F., R.W. Carlson, R.J. Walker, M. Jackson, M. Garçon, and M. Norman, *Tracking Hadean processes in modern basalts with 142-Neodymium.* Earth and Planetary Science Letters, 2018. **484**: p. 184-191.
17. Mundl-Petermeier, A., R.J. Walker, R.A. Fischer, V. Lekic, M.G. Jackson, and M.D. Kurz, *Anomalous 182W in high 3He/4He ocean island basalts: Fingerprints of Earth's core?* Geochimica et Cosmochimica Acta, 2020. **271**: p. 194-211.
18. Williams, C.D. and S. Mukhopadhyay, *Capture of nebular gases during Earth's accretion is preserved in deep-mantle neon.* Nature, 2019. **565**(7737): p. 78-81.
19. O'Neil, J., R.W. Carlson, D. Francis, and R.K. Stevenson, *Neodymium-142 Evidence for Hadean Mafic Crust.* Science, 2008. **321**: p. 1828-1831.
20. Jackson, M.G., T.W. Becker, and J.G. Konter, *Evidence for a deep mantle source for EM and HIMU domains from integrated geochemical and geophysical constraints.* Earth and Planetary Science Letters, 2018. **484**: p. 154-167.

21. Gülcher, A.J.P., M.D. Ballmer, and P.J. Tackley, *Coupled dynamics and evolution of primordial and recycled heterogeneity in Earth's lower mantle.* Solid Earth, 2021. **12**(9): p. 2087-2107.
22. Koppers, A.A.P., T.W. Becker, M.G. Jackson, K. Konrad, R.D. Müller, B. Romanowicz, B. Steinberger, and J.M. Whittaker, *Mantle plumes and their role in Earth processes.* Nature Reviews Earth & Environment, 2020. **2**: p. 382-401.
23. Jones, T.D., R.R. Maguire, P.E. van Keken, J. Ritsema, and P. Koelemeijer, *Subducted oceanic crust as the origin of seismically slow lower-mantle structures.* Progress in Earth and Planetary Science, 2020. **7**(1).
24. Jackson, M.G., T.W. Becker, and B. Steinberger, *Spatial Characteristics of Recycled and Primordial Reservoirs in the Deep Mantle.* Geochemistry, Geophysics, Geosystems, 2021. **22**(3).
25. Giuliani, A., M.G. Jackson, A. Fitzpayne, and H. Dalton, *Remnants of early Earth differentiation in the deepest mantle-derived lavas.* Proc Natl Acad Sci U S A, 2021. **118**(1).
26. Chauvel, C., A.W. Hofmann, and P. Vidal, *HIMU-EM: The French Polynesian connection.* Earth and Planetary Science Letters, 1992. **110**: p. 99-119.
27. Chauvel, C., R.C. Maury, S. Blais, E. Lewin, H. Guillou, G. Guille, P. Rossi, and M.-A. Gutscher, *The size of plume heterogeneities constrained by Marquesas isotopic stripes.* Geochemistry, Geophysics, Geosystems, 2012. **13**(7): p. n/a-n/a.
28. Nicklas, R.W., J.M.D. Day, T.D. Jones, and P.R. Castillo, *Evidence for a primitive deep mantle component in the source of Marquesas Islands Lavas from Os isotope and highly siderophile element abundance systematics.* Geochimica et Cosmochimica Acta, 2022. **329**: p. 51-69.
29. Stracke, A., *Earth's heterogeneous mantle: A product of convection-driven interaction between crust and mantle.* Chemical Geology, 2012. **330-331**: p. 274-299.
30. Herret, M.T., B.J. Peters, D. Kim, P.R. Castillo, and A. Mundl-Petermeier, *Decoupling of short-lived radiogenic and helium isotopes in the Marquesas hotspot.* Chemical Geology, 2023. **640**.
31. Friedman, A.M., J. Milsted, D. Metta, D. Henderson, J. Lerner, A.L. Harkness, and D.J. Rokop, *Alpha decay half lives of 148Gd, 150Gd, and 146Sm.* Radiochimica Acta, 1966. **5**(4): p. 192-194.
32. Tanaka, T., S. Togashi, H. Kamioka, H. Amakawa, H. Kagami, T. Hamamoto, M. Zuhara, Y. Orihashi, S. Yoneda, H. Shimizu, T. Kunimaru, K. Takahashi, T. Zanagi, T. Nakano, H. Fujimaki, R. Shinjo, Y. Asahara, M. Tanimizu, and C. Dragusanu, *JNdi-1: a neodymium isotopic reference in consistency with LaJolla neodymium.* Chemical Geology, 2000. **168**: p. 279-281.
33. Ludwig, K.R., *Isoplot 3.00: A geochronological toolkit for Microsoft Excel*. 2003, Berkeley Geochronology Center. p. 1-70.
34. Jackson, M.G., S.R. Hart, A.A. Koppers, H. Staudigel, J. Konter, J. Blusztajn, M. Kurz, and J.A. Russell, *The return of subducted continental crust in Samoan lavas.* Nature, 2007. **448**(7154): p. 684-7.
35. Stracke, A., M. Willig, F. Genske, P. Béguelin, and E. Todd, *Chemical Geodynamics Insights From a Machine Learning Approach.* Geochemistry, Geophysics, Geosystems, 2022. **23**(10).
36. O'Neil, J. and R.W. Carlson, *Building Archean cratons from Hadean mafic crust.* Science, 2017. **355**: p. 1199-1202.
37. Stracke, A., A.W. Hofmann, and S.R. Hart, *FOZO, HIMU, and the rest of the mantle zoo.* Geochemistry, Geophysics, Geosystems, 2005. **6**(5).
38. Jackson, M.G., T.W. Becker, and J.G. Konter, *Geochemistry and Distribution of Recycled Domains in the Mantle Inferred From Nd and Pb Isotopes in Oceanic Hot Spots: Implications for Storage in the Large Low Shear Wave Velocity Provinces.* Geochemistry, Geophysics, Geosystems, 2018. **19**(9): p. 3496-3519.
39. Willbold, M. and A. Stracke, *Formation of enriched mantle components by recycling of upper and lower continental crust.* Chemical Geology, 2010. **276**(3-4): p. 188-197.
40. Castillo, P.R., P. Scarsi, and H. Craig, *He, Sr, Nd, and Pb isotopic constraints on the origin of the Marquesas and other linear volcanic chains.* Chemical Geology, 2007. **240**(3-4): p. 205-221.

41. Hanyu, T. and I. Kaneoka, *The uniform and low 3He/4He ratios of HIMU basalts as evidence for their origin as recycled materials.* Nature, 2007. **390**: p. 273-276.
42. Jackson, M.G., J. Blichert-Toft, S.A. Halldorsson, A. Mundl-Petermeier, M. Bizimis, M.D. Kurz, A.A. Price, S. Harethardottir, L.N. Willhite, K. Breddam, T.W. Becker, and R.A. Fischer, *Ancient helium and tungsten isotopic signatures preserved in mantle domains least modified by crustal recycling.* Proc Natl Acad Sci U S A, 2020. **117**(49): p. 30993-31001.
43. Plank, T. and C.H. Langmuir, *The chemical composition of subducting sediment and its consequences for the crust and mantle.* Chemical Geology, 1998. **145**: p. 325-394.
44. Bennett, V.C., A.D. Brandon, and A.P. Nutman, *Coupled 142Nd-143Nd Isotopic Evidence for Hadean Mantle Dynamics.* Science, 2007. **318**: p. 1907-1910.
45. O'Neil, J., H. Rizo, M. Boyet, R.W. Carlson, and M.T. Rosing, *Geochemistry and Nd isotopic characteristics of Earth's Hadean mantle and primitive crust.* Earth and Planetary Science Letters, 2016. **442**: p. 194-205.
46. Boyet, M. and R. Carlson, *A new geochemical model for the Earth's mantle inferred from 146Sm–142Nd systematics.* Earth and Planetary Science Letters, 2006. **250**(1-2): p. 254-268.
47. Wasilewski, B., J. O'Neil, and H. Rizo, *Archean crustal evolution of the Saglek-Hebron Complex, Northern Labrador, revealed from coupled 147–146Sm-143–142Nd systematics.* Earth and Planetary Science Letters, 2022. **594**.
48. Hyung, E. and S.B. Jacobsen, *The (142)Nd/(144)Nd variations in mantle-derived rocks provide constraints on the stirring rate of the mantle from the Hadean to the present.* Proc Natl Acad Sci U S A, 2020. **117**(26): p. 14738-14744.
49. Rizo, H., M. Boyet, J. Blichert-Toft, J. O'Neil, M.T. Rosing, and J.L. Paquette, *The elusive Hadean enriched reservoir revealed by 142Nd deficits in Isua Archaean rocks.* Nature, 2012. **491**(7422): p. 96-100.
50. Nebel, O., F.A. Capitanio, J.F. Moyen, R.F. Weinberg, F. Clos, Y.J. Nebel-Jacobsen, and P.A. Cawood, *When crust comes of age: on the chemical evolution of Archaean, felsic continental crust by crustal drip tectonics.* Philos Trans A Math Phys Eng Sci, 2018. **376**(2132).
51. Klein, B.Z., O. Jagoutz, and M.D. Behn, *Archean crustal compositions promote full mantle convection.* Earth and Planetary Science Letters, 2017. **474**: p. 516-526.
52. Konhauser, K.O., N.J. Planavsky, D.S. Hardisty, L.J. Robbins, T.J. Warchola, R. Haugaard, S.V. Lalonde, C.A. Partin, P.B.H. Oonk, H. Tsikos, T.W. Lyons, A. Bekker, and C.M. Johnson, *Iron formations: A global record of Neoarchaean to Palaeoproterozoic environmental history.* Earth-Science Reviews, 2017. **172**: p. 140-177.
53. Agić, H., M. Moczydłowska, and L. Yin, *Diversity of organic-walled microfossils from the early Mesoproterozoic Ruyang Group, North China Craton – A window into the early eukaryote evolution.* Precambrian Research, 2017. **297**: p. 101-130.
54. Yin, A., *An episodic slab-rollback model for the origin of the Tharsis rise on Mars: Implications for initiation of local plate subduction and final unification of a kinematically linked global plate-tectonic network on Earth.* Lithosphere, 2012. **4**(6): p. 553-593.
55. Davaille, A., S.E. Smrekar, and S. Tomlinson, *Experimental and observational evidence for plume-induced subduction on Venus.* Nature Geoscience, 2017. **10**(5): p. 349-355.
56. Bouvier, A., J.D. Vervoort, and P.J. Patchett, *The Lu–Hf and Sm–Nd isotopic composition of CHUR: Constraints from unequilibrated chondrites and implications for the bulk composition of terrestrial planets.* Earth and Planetary Science Letters, 2008. **273**(1-2): p. 48-57.
57. Graham, D.W., *Noble Gas Isotope Geochemistry of Mid-Ocean Ridge and Ocean Island Basalts: Characterization of Mantle Source Reservoirs.* Reviews in Mineralogy and Geochemistry, 2002. **47**(1): p. 247-317.

58. Caro, G., P. Morino, S.J. Mojzsis, N.L. Cates, and W. Bleeker, *Sluggish Hadean geodynamics: Evidence from coupled 146,147 Sm– 142,143 Nd systematics in Eoarchean supracrustal rocks of the Inukjuak domain (Québec).* Earth and Planetary Science Letters, 2017. **457**: p. 23-37.
59. Morino, P., G. Caro, L. Reisberg, and A. Schumacher, *Chemical stratification in the post-magma ocean Earth inferred from coupled 146,147Sm–142,143Nd systematics in ultramafic rocks of the Saglek block (3.25–3.9 Ga; northern Labrador, Canada).* Earth and Planetary Science Letters, 2017. **463**: p. 136-150.
60. Duncan, R.A. and I. McDougall, *Migration of volcanism with time in the Marquesas Islands, French Polynesia.* Earth and Planetary Science Letters, 1974. **21**: p. 414-420.
61. Kim, D., B. Ménard, D. Baron, and M. Taghizadeh-Popp, *Sequencing seismograms: A panoptic view of scattering in the core-mantle boundary region.* Science, 2020. **368**: p. 1223-1228.
62. Dupuy, C., P. Vidal, H.G. Barsczus, and C. Chauvel, *Origin of basalts from the Marquesas Archipelago (south central Pacific Ocean): isotope and trace element constraints.* Earth and Planetary Science Letters, 1987. **82**: p. 145-152.
63. Woodhead, J.D., *Temporal geochemical evolution in oceanic intra-plate volcanics: a case study from the Marquesas (French Polynesia) and comparison with other hotspots.* Contributions to Mineralogy and Petrology, 1992. **111**: p. 458-467.
64. Desonie, D.L., R.A. Duncan, and J.H. Natland, *Temporal and geochemical variability of volcanic products of the Marquesas Hotspot.* Journal of Geophysical Research: Solid Earth, 1993. **98**(B10): p. 17649-17665.
65. Jackson, M., M. Kurz, S. Hart, and R. Workman, *New Samoan lavas from Ofu Island reveal a hemispherically heterogeneous high 3He/4He mantle.* Earth and Planetary Science Letters, 2007. **264**(3-4): p. 360-374.
66. Woodhead, J.D., *Extreme HIMU in an oceanic setting: the geochemistry of Mangaia Island (Polynesia), and temporal evolution of the Cook-Austral hotspot.* Journal of Volcanology and Geothermal Research, 1996. **72**: p. 1-19.
67. Garçon, M., M. Boyet, R.W. Carlson, M.F. Horan, D. Auclair, and T.D. Mock, *Factors influencing the precision and accuracy of Nd isotope measurements by thermal ionization mass spectrometry.* Chemical Geology, 2018. **476**: p. 493-514.
68. Chu, Z.-Y., M.-J. Wang, C.-F. Li, Y.-H. Yang, J.-J. Xu, W. Wang, and J.-H. Guo, *Separation of Nd from geological samples by a single TODGA resin column for high precision Nd isotope analysis as NdO+ by TIMS.* Journal of Analytical Atomic Spectrometry, 2019. **34**(10): p. 2053-2060.
69. Wang, D. and R.W. Carlson, *Tandem-column extraction chromatography for Nd separation: minimizing mass-independent isotope fractionation for ultrahigh-precision Nd isotope-ratio analysis.* Journal of Analytical Atomic Spectrometry, 2022. **37**(1): p. 185-193.
70. Jochum, K.P., U. Nohl, K. Herwig, E. Lammel, B. Stoll, and A.W. Hofmann, *GeoReM: A New Geochemical Database for Reference Materials and Isotopic Standards.* Geostandards and Geoanalytical Research, 2005. **29**(3): p. 333-338.
71. Saji, N.S., D. Wielandt, C. Paton, and M. Bizzarro, *Ultra-high-precision Nd-isotope measurements of geological materials by MC-ICPMS.* J Anal At Spectrom, 2016. **31**(7): p. 1490-1504.
72. Andreasen, R. and M. Sharma, *Fractionation and mixing in a thermal ionization mass spectrometer source: Implications and limitations for high-precision Nd isotope analyses.* International Journal of Mass Spectrometry, 2009. **285**(1-2): p. 49-57.
73. Peters, B.J., R.W. Carlson, J.M.D. Day, and M.F. Horan, *Hadean silicate differentiation preserved by anomalous (142)Nd/(144)Nd ratios in the Reunion hotspot source.* Nature, 2018. **555**(7694): p. 89-93.
74. Peters, B.J., A. Mundl-Petermeier, R.W. Carlson, R.J. Walker, and J.M.D. Day, *Combined Lithophile-Siderophile Isotopic Constraints on Hadean Processes Preserved in Ocean Island Basalt Sources.* Geochemistry, Geophysics, Geosystems, 2021. **22**(3).

75. Peters, B.J., J.M.D. Day, and L.A. Taylor, *Early mantle heterogeneities in the Réunion hotspot source inferred from highly siderophile elements in cumulate xenoliths.* Earth and Planetary Science Letters, 2016. **448**: p. 150-160.
76. Zhang, Y. and Y. Liu, *How to produce isotope anomalies in mantle by using extremely small isotope fractionations: A process-driven amplification effect?* Geochimica et Cosmochimica Acta, 2020. **291**: p. 19-49.
77. Baker, J., D. Peate, T. Waight, and C. Meyzen, *Pb isotopic analysis of standards and samples using a 207Pb–204Pb double spike and thallium to correct for mass bias with a double-focusing MC-ICP-MS.* Chemical Geology, 2004. **211**(3-4): p. 275-303.
78. McDonough, W.F. and S.-s. Sun, *The composition of the Earth.* Chemical Geology, 1995. **120**: p. 223-253.
79. Rudnick, R.L. and S. Gao, *Composition of the continental crust*, in *Treatise on Geochemistry*, H.D. Holland and K.K. Turekian, Editors. 2003, Elsevier. p. 1-64.
80. Plank, T., *The Chemical Composition of Subducting Sediments*, in *Treatise on Geochemistry*. 2014. p. 607-629.
81. Rizo, H., M. Boyet, J. Blichert-Toft, and M.T. Rosing, *Early mantle dynamics inferred from 142Nd variations in Archean rocks from southwest Greenland.* Earth and Planetary Science Letters, 2013. **377-378**: p. 324-335.
82. McCulloch, M.T. and G.J. Wasserburg, *Sm-Nd and Rb-Sr Chronology of Continental Crust Formation.* Science, 1978. **200**: p. 1003-1011.
83. Garapić, G., M.G. Jackson, E.H. Hauri, S.R. Hart, K.A. Farley, J.S. Blusztajn, and J.D. Woodhead, *A radiogenic isotopic (He-Sr-Nd-Pb-Os) study of lavas from the Pitcairn hotspot: Implications for the origin of EM-1 (enriched mantle 1).* Lithos, 2015. **228-229**: p. 1-11.
84. Millot, R., C.-J. Allègre, J. Gaillardet, and S. Roy, *Lead isotopic systematics of major river sediments: a new estimate of the Pb isotopic composition of the Upper Continental Crust.* Chemical Geology, 2004. **203**(1-2): p. 75-90.
85. Reimink, J.R., T. Chacko, R.W. Carlson, S.B. Shirey, J. Liu, R.A. Stern, A.M. Bauer, D.G. Pearson, and L.M. Heaman, *Petrogenesis and tectonics of the Acasta Gneiss Complex derived from integrated petrology and 142Nd and 182W extinct nuclide-geochemistry.* Earth and Planetary Science Letters, 2018. **494**: p. 12-22.
86. Andreasen, R., M. Sharma, K.V. Subbarao, and S.G. Viladkar, *Where on Earth is the enriched Hadean reservoir?* Earth and Planetary Science Letters, 2008. **266**(1-2): p. 14-28.
87. Archer, G.J., G.A. Brennecka, P. Gleißner, A. Stracke, H. Becker, and T. Kleine, *Lack of late-accreted material as the origin of 182W excesses in the Archean mantle: Evidence from the Pilbara Craton, Western Australia.* Earth and Planetary Science Letters, 2019. **528**.
88. Caro, G., B. Bourdon, J.-L. Birck, and S. Moorbath, *High-precision 142Nd/144Nd measurements in terrestrial rocks: Constraints on the early differentiation of the Earth's mantle.* Geochimica et Cosmochimica Acta, 2006. **70**(1): p. 164-191.
89. Cipriani, A., E. Bonatti, and R.W. Carlson, *Nonchondritic142Nd in suboceanic mantle peridotites.* Geochemistry, Geophysics, Geosystems, 2011. **12**(3): p. n/a-n/a.
90. de Leeuw, G.A.M., R.M. Ellam, F.M. Stuart, and R.W. Carlson, *142Nd/144Nd inferences on the nature and origin of the source of high 3He/4He magmas.* Earth and Planetary Science Letters, 2017. **472**: p. 62-68.
91. O'Neill, C., V. Debaille, and W. Griffin, *Deep earth recycling in the Hadean and constraints on surface tectonics.* American Journal of Science, 2013. **313**(9): p. 912-932.
92. Jackson, M.G. and R.W. Carlson, *Homogeneous superchondritic142Nd/144Nd in the mid-ocean ridge basalt and ocean island basalt mantle.* Geochemistry, Geophysics, Geosystems, 2012. **13**(6): p. n/a-n/a.

93. Maltese, A., G. Caro, O.P. Pandey, D. Upadhyay, and K. Mezger, *Direct evidence for crust-mantle differentiation in the late Hadean.* Communications Earth & Environment, 2022. **3**(1).
94. Mei, Q.-F., J.-H. Yang, C.-F. Li, X.-C. Wang, J. Konnunaho, Y.-D. Wu, H. Zhong, Y.-G. Xu, and H. Wang, *Modern ocean island basalt–like 182W signature in Paleoarchean mafic rocks: Implications for the generation, preservation, and destruction of early mantle heterogeneities.* Geology, 2023. **51**(10): p. 919-923.
95. Murphy, D.T., A.D. Brandon, V. Debaille, R. Burgess, and C. Ballentine, *In search of a hidden long-term isolated sub-chondritic 142Nd/144Nd reservoir in the deep mantle: Implications for the Nd isotope systematics of the Earth.* Geochimica et Cosmochimica Acta, 2010. **74**(2): p. 738-750.
96. Murphy, D., H. Rizo, J. O'Neil, R. Hepple, D. Wiemer, A. Kemp, and J. Vervoort, *Combined Sm-Nd, Lu-Hf, and 142Nd study of Paleoarchean basalts from the East Pilbara Terrane, Western Australia.* Chemical Geology, 2021. **578**.
97. Puchtel, I.S., J. Blichert-Toft, M. Touboul, M.F. Horan, and R.J. Walker, *The coupled182W-142Nd record of early terrestrial mantle differentiation.* Geochemistry, Geophysics, Geosystems, 2016. **17**(6): p. 2168-2193.
98. Reimink, J.R., J.H.F.L. Davies, A.M. Bauer, and T. Chacko, *A comparison between zircons from the Acasta Gneiss Complex and the Jack Hills region.* Earth and Planetary Science Letters, 2020. **531**.
99. Rizo, H., M. Boyet, J. Blichert-Toft, and M. Rosing, *Combined Nd and Hf isotope evidence for deep-seated source of Isua lavas.* Earth and Planetary Science Letters, 2011. **312**(3-4): p. 267-279.
100. Roth, A.S.G., E.E. Scherer, C. Maden, K. Mezger, and B. Bourdon, *Revisiting the 142Nd deficits in the 1.48 Ga Khariar alkaline rocks, India.* Chemical Geology, 2014. **386**: p. 238-248.
101. Roth, A.S.G., B. Bourdon, S.J. Mojzsis, M. Touboul, P. Sprung, M. Guitreau, and J. Blichert-Toft, *Inherited 142Nd anomalies in Eoarchean protoliths.* Earth and Planetary Science Letters, 2013. **361**: p. 50-57.
102. Saji, N.S., K. Larsen, D. Wielandt, M. Schiller, M.M. Costa, M.J. Whitehouse, M.T. Rosing, and M. Bizzarro, *Hadean geodynamics inferred from time-varying (142)Nd/(144)Nd in the early Earth rock record.* Geochem Perspect Lett, 2018. **7**: p. 43-48.
103. Schneider, K.P., J.E. Hoffmann, M. Boyet, C. Münker, and A. Kröner, *Coexistence of enriched and modern-like 142Nd signatures in Archean igneous rocks of the eastern Kaapvaal Craton, southern Africa.* Earth and Planetary Science Letters, 2018. **487**: p. 54-66.
104. Wainwright, A.N., F. El Atrassi, V. Debaille, and N. Mattielli, *Geochemistry and petrogenesis of Archean mafic rocks from the Amsaga area, West African craton, Mauritania.* Precambrian Research, 2019. **324**: p. 208-219.